

MSc Chemistry
Science for Energy and
Sustainability

Master Thesis

**Energy transfer processes in ytterbium doped
metal halide perovskites probed with
cathodoluminescence**

by

Heleen Groenewegen
11021101

22 October 2021

48 EC

January – October 2021

Supervisor/Examiner:
Prof. Dr. Albert Polman

Examiner:
Dr. René Williams

Daily supervisors:
Nika van Nielen, MSc

Abstract

Quantum cutting (QC) can minimize losses in c-Si solar cells by converting one high energy photon into two low energy photons. Yb^{3+} -doped CsPbCl_3 is able to perform quantum cutting due to the favorable combination of absorption wavelength of the perovskite (415 nm) and the emission wavelength of the Yb (975 nm). Cathodoluminescence was used to study the optical properties of Yb^{3+} -doped CsPbCl_3 and the perovskite-Yb energy transfer process. CL is the emission of optical radiation by a material in response to excitation by incident high-energy electrons. To the best of our knowledge, this work presents for the first time spatially resolved CL emission spectra and CL decay traces of CsPbCl_3 and Yb-doped CsPbCl_3 encapsulated in a silica matrix. With the high spatial resolution of CL measurements local variations in luminescence and lifetime could be determined, providing more information about the samples at the nanoscale. To examine how QC behaves in Yb^{3+} -doped CsPbCl_3 when probed with CL, both CL emission spectra and CL decay traces were studied. The excitation of the optically forbidden excited state of the Yb ions is likely the result of both QC and self-excitation by incident high energy electrons. The results showed several indications for energy transfer from the perovskite host to the excited state of Yb, however quantifying to what extent QC is responsible for excitation of Yb was not feasible. The encapsulation in silica molecular sieves was found to be very successful for electron-based studies. This work also introduced a method to measure longer CL lifetimes within our set-up and the emissive lifetime of the $^2\text{F}_{5/2} \rightarrow ^2\text{F}_{7/2}$ transition of Yb^{3+} could therefore be measured.

CL

Table of contents

Introduction	4
1. Ytterbium doped perovskites	6
1.1 Perovskite structure	6
1.2 Lanthanide doping	7
1.3 Quantum cutting in Yb^{3+} -doped CsPbCl_3	9
2. Cathodoluminescence imaging	11
2.1 Electron microscopy	11
2.2 Experimental set-up	12
2.3 Impact of electron beam on perovskites	15
3. Results & Discussion	17
3.1 Secondary electron images of molecular sieves	17
3.2 Spatially resolved CL emission spectra	17
3.3 Time-resolved CL decay traces and maps of CsPbCl_3	23
3.4 Time-resolved CL decay traces of Yb^{3+}	24
3.5 CL $g^{(2)}(\tau)$ measurements	25
Conclusion & Outlook	27
Acknowledgement	28
References	29

Introduction

The alarming shift in climate patterns is mainly caused by the exponential rise in greenhouse gas emissions, coming from the extensive use of fossil fuels over the past centuries.¹ As climate change worsens and the worldwide demand for energy increases, the use of efficient renewable energy technologies becomes more important. The abundant energy of the sun is in principle enough to supply the whole world with renewable energy.² Photovoltaic (PV) materials convert photons into electricity using semiconducting materials.² Crystalline silicon (c-Si) is the most abundant used PV material, however it is reaching its theoretical limit. Moreover, there is a mismatch between the incident solar spectrum and the absorption spectrum of silicon, which results in major energy loss.³ Photons with energies larger than the silicon band gap are absorbed, but the excess energy is lost to the creation of phonons. Therefore only a fraction of the incident solar spectrum is used to produce electricity and cell efficiency is limited.³

To make more efficient use of the solar spectrum, recent research focuses on incorporating down-converting materials into a thin transparent layer on top of the solar cell.^{4,5} Down-conversion (DC) is the process of converting one incident high-energy photon into two or more low energy photons.⁶ This down-conversion of photons can lead to quantum efficiencies of more than 100% and is therefore also referred to as quantum cutting (QC).⁷ Figure 1 plots the global standard solar spectrum and the fractions that can be absorbed by c-Si (green).⁷ Analysis of the energy content of this spectrum shows that DC can potentially result in the absorption of an extra 15% of the total solar spectrum, which would normally be lost to thermalization.⁸

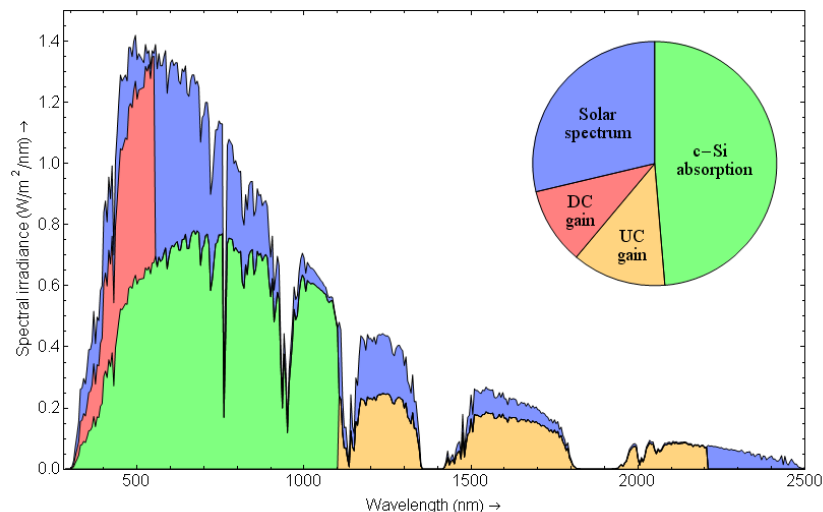


Figure 1. AM1.5G solar spectrum (purple) showing the conversion of the absorbed part of the solar spectrum for a c-Si solar cell (green) and the potential gain for DC (red) and up conversion (UC, yellow), which is outside the scope of this thesis. The potential gain for DC reflects the extra energy that can be absorbed by Si if every photon with an energy higher than two times the Si band gap is converted into two photons in the near infrared range where absorption by Si is very efficient. Note that the figure considers no other losses than spectral mismatch losses. Figure taken from Ref. 7.

To increase the efficiency of c-Si solar cells with DC, it is important to study materials with rich energy level structures that allow for efficient modification of the incident solar spectrum. Doped perovskites are one of the most promising materials for DC and in the past few years they have become the subject of extensive research interest due to their potential for high-efficiency and low-cost solar cells which allows for large scale application.^{7,9} One of the many interesting and promising fundamental photovoltaic properties of perovskite solar cells (PSCs) is the possibility to alter the versatile chemical composition of the perovskite lattice and consequently tune the intrinsic band gap.¹⁰ In recent research there has been growing interest in lanthanide-doped perovskites as a way to introduce new optical, electronic and other capabilities.^{9,11,12} Lanthanide ions are in general optically active elements that can provide energy levels within the band gap of the material and therefore can induce the appearance of

optical transitions at energies lower than that of the fundamental absorption.¹² The absorption and emission at these various energy levels allows for DC processes.¹³

DC in lanthanide-doped perovskites have been studied with photoluminescence (PL) and various other optical characterization techniques to gain more insights into the energy-transfer processes and carrier dynamics.^{3,14–16} However, these carrier dynamics can also be studied by excitation with fast electrons and can give insights in the electron-matter interaction.^{17–19} Cathodoluminescence (CL) is the emission of optical radiation by a material in response to excitation by incident high-energy electrons, similarly to how materials can be excited by incident photons in PL.²⁰ CL is a powerful method to optically characterize nanostructured materials with the deep-subwavelength resolution and CL measurements can identify compositional variations derived from spatial maps with nanometer resolution based on luminescence variations.²⁰ CL emission can be used to explore many fundamental properties of matter that cannot be obtained using optical excitation and it therefore has broad areas of applications, as is described later in more detail. An application of particular interest to this thesis is the study of temporal dynamics of carrier diffusion and recombination as well as the statistics of light emission processes via the time resolved collection and analysis of the emitted light.

CL can play an important role in revealing properties of doped perovskites and expand the fundamental understanding of this new group of functional materials. Perovskite materials have stability issues and are known to be very fragile.²¹ This gives a substantial number of challenges for the development of perovskites toward practical applications. Electron beam studies on perovskites can give more insights into the impact of electrons on the structural stability, to guide future design of more robust perovskites.

This thesis focuses on cesium lead chloride perovskites (CsPbCl_3), both undoped and doped with ytterbium (Yb) ions, that are encapsulated in a silica matrix for improved stability. CL is used to study the decay traces and spontaneous emission statistics of electron-excited carriers. To the best of our knowledge, this is the first work that presents spatially resolved CL emission spectra and CL decay traces of the studied halide perovskites. These measurements can give fundamental insights about the optical properties of these materials and the quantum cutting mechanisms. The aim of this work is to gain a better understanding of the energy transfer processes and carrier dynamics in these specific materials and to evaluate how the sample reacts to incident electrons of different energies. With the high spatial resolution of CL measurements local variations in luminescence and lifetime can be determined and can give more information at the nanoscale. Besides expanding the current framework of knowledge on lanthanide doped perovskites, this work also aims to give more insight into the technical potential of the CL technique used to study emission dynamics in lanthanide doped perovskite composites.

In the first Chapter of this thesis a theoretical framework is given in which the characteristics of both perovskite and ytterbium are addressed and quantum cutting in this specific material is explained. In Chapter 2, cathodoluminescence imaging as well as the experimental set-up is described, and specific newfound features are explained. In Chapter 3 the CL emission spectra are shown to analyze spectral characteristics of the doped and undoped CsPbCl_3 upon excitation by incident electrons of different current and to identify microstructural information with regions of enhanced emission. Additionally, the dynamics of carriers in the perovskite samples and variations in luminescent lifetimes are discussed based on time-resolved cathodoluminescence (TR-CL) imaging. Subsequently lifetime measurements for Yb are shown and discussed. In the final Chapter, these results are summarized and an outlook for further research is presented.

1. Ytterbium doped perovskites

In photovoltaic (PV) materials only photons with energies above the bandgap get absorbed, but all excess energy of high-energy photons is converted into heat, a loss known as thermalization loss or quantum defect.²² Quantum cutting can minimize this loss by transforming high energy photons into multiple low energy photons. Figure 1.1 shows a diagram of how a simplified QC layer can be placed on top of a PV material. This layer absorbs high energy photons and emits converted low energy photons, while also transmitting other lower energy incident photons that were not absorbed by the QC layer. In this way an additional part of the solar spectrum can be absorbed efficiently by the PV layer.

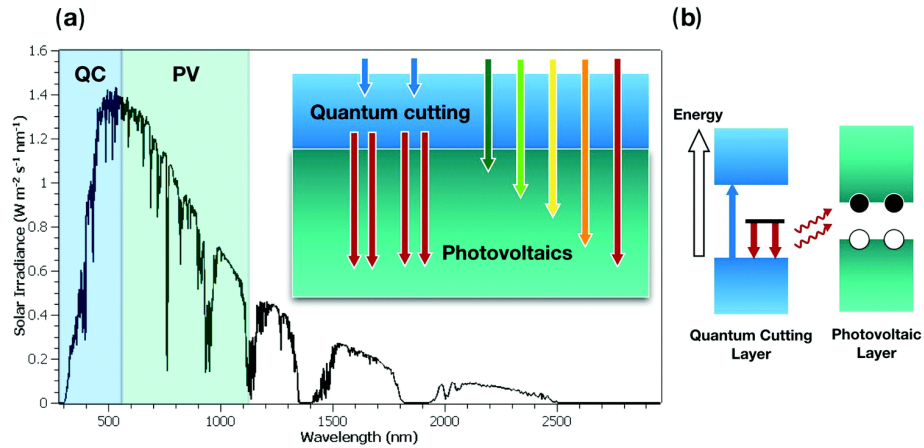


Figure 1.1. (a) Solar spectrum with highlighted regions for ideal quantum cutting and photovoltaics absorption. The schematic in the inset shows a simplified QC-PV architecture. (b) General mechanism of a QC layer in combination with a PV layer in which the lower band gap material in the QC layer emits two photons that can be absorbed by the PV layer. Figure taken from Ref. 22.

With the QC layer a theoretical photoluminescence quantum yield (PLQY) of 200% can be reached if the emitted photons are half the hosts' bandgap energy and every incident high energy photon is converted into two low energy photons. Quantum yield is defined by Equation 1.1.

$$\Phi = \frac{N(\text{photons emitted})}{N(\text{photons absorbed})} \quad \text{Eq. 1.1}$$

$\text{Yb}^{3+}:\text{CsPbCl}_3$ is an excellent QC system for Si-based solar cells, because of the match of the absorption wavelength (415 nm or 2.99 eV) of the perovskite and emission wavelength of the Yb ions (984 nm or 1.26 eV), which is right above the c-Si bandgap (1.1 eV).²²

In order to gain a better understanding of the quantum cutting process in Yb-doped CsPbCl_3 , first the perovskite structure as well as the lanthanide doping process is explained. Subsequently, different proposed energy-transfer models of the system are explained and discussed.

1.1 Perovskite structure

The perovskite crystal lattice structure exhibits a ABX_3 base configuration, which is depicted in Figure 1.2.

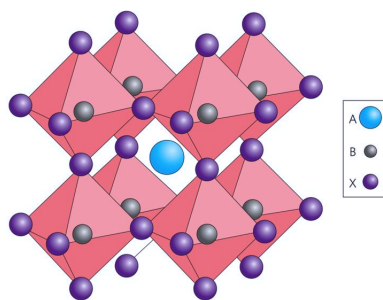


Figure 1.2. Schematic crystal structure of ABX_3 perovskite lattice arrangement. Figure taken from Ref. 10.

Such a structure consists of a monovalent organic or inorganic cation A, surrounded by a network of octahedra consisting of a central metal cation B and six halogen anions (X).^{7,10,11} By altering the composition of the lattice, the optical and electronic properties can be controlled, which can lead to tunable bandgap and enhanced quantum yields.¹⁶ The fundamental properties can also be modified by intentionally introducing heteroatoms into the target lattice, also referred to as doping.¹⁶ Doping in general does not change the host crystal structure and basic characteristics much, since only a small amount of impurities are introduced to the lattice.¹⁶ This work focuses on the metal halide perovskite $CsPbCl_3$, that has a bandgap of 2.99 eV (415 nm).²² The band edge emission has a reported average PL lifetime of a few nanoseconds.^{9,23–25}

1.2 Lanthanide doping

Lanthanides are the elements 57 (La) to 71 (Lu) in the periodic table and have been widely explored as optically active dopants.^{12,26} Their 4f inner shell is filled with up to 14 electrons and they usually occur in their trivalent form (Ln^{3+}). Doping trivalent lanthanide ions into all-inorganic $CsPbX_3$ (with $X = Cl$ or Cl/Br) perovskite nanocrystals have been found to be very suitable, since the octahedral coordination is compatible for Ln^{3+} doping.¹² Over the past three years, remarkable success has been achieved with Yb-doped perovskites, combining the optoelectronic properties of the perovskite host with the electronic transitions of the dopants. Especially Yb³⁺-doped $CsPbCl_3$ nanocrystals and thin films have shown exceptional high PLQY due to down-conversion.²² Doping with other lanthanides, such as Eu³⁺, has also been explored.^{25,27} Eu³⁺ has multiple radiative transitions between the 5D_0 excited state and the 7F_J manifold, that show emission in the range of 600 to 700 nm.²⁷ Down-conversion is not possible for this system, however the energy transfer process between host and Eu³⁺ ions is described as down-shifting.⁷ During this process only one low energy photon is emitted for one incident high energy photon and energy is lost due to non-radiative relaxation. This also results in a lower PLQY for these systems when compared with Yb³⁺-doped perovskites.²⁵

1.2.1 Ytterbium transition

Yb is an element of the lanthanide series with atomic number 70 and is also commonly referred to as rare earth element. However, it is not rare in terms of average crystal abundance, instead the concentrated deposits are limited in number.²⁸ Trivalent ytterbium ions (Yb³⁺) have a valence electron configuration of $4f^{13}5s^25p^6$, and these atomic states are crucial to understand the DC process in Yb-based materials. The partially filled 4f shell is shielded from the surroundings by the filled 5s² and 5p⁶ orbitals and is therefore relatively stable, which is essential for the DC process.²⁹ Yb³⁺ has one optical transitions, between the $^2F_{5/2}$ and $^2F_{7/2}$ energy levels, with an energy difference of 975 nm or 1.27 eV.²² Theoretically, such $4f \rightarrow 4f$ transitions are not allowed under the Laporte rule, stating that transitions between symmetrical atomic orbitals (*s-s*, *p-p*, *d-d*, *f-f*) are parity forbidden.²⁹ This means that inversion of the sign of one or all spatial coordinates is not allowed and therefore Laporte forbidden transitions are very weak.²² Nevertheless, small changes in symmetry of the orbital configuration, as a result of admixture of opposite parity states upon introduction to a host material, provide alteration from the intrinsic symmetry which makes the transfer slightly allowed.²⁹ A higher covalence of the host, which can also be described as a less electron negative host that can share its bonding electrons for a covalent bond, makes the forbidden transition more allowed. This is because the energy difference between electronic

transitions between energy levels, which are determined by electron interactions, becomes smaller.²⁹ Ultimately this results in a stronger absorption band. The partially forbidden character of the transition makes it possible that an excitonic transition from a host, for example a perovskite crystal, to Yb^{3+} may lead to population of the $^2\text{F}_{5/2}$ state.²² The excited state is then long-lived, but eventually emits a low-energy photon with high efficiency.²² Literature reports slightly different average PL lifetimes for this Yb^{3+} transition, depending on the host composition and different Yb^{3+} concentrations. In CsPbCl_3 nanocrystals (NC) determined lifetimes vary from 589 μs and 941.9 μs to over 2 ms.^{23–25,30} In other systems, such as lanthanide fibers, lifetimes from 470 to 830 μs were found.³¹

1.2.2 Ytterbium incorporation in the perovskite crystal lattice

For incorporation of Yb^{3+} in the perovskite lattice the Yb ion partially replace another ion. *Pan et al.* performed density functional theory (DFT) calculations in previous studies to investigate the position possibilities of the Yb^{3+} ion.²⁵ The formation energies of three different defects in the perovskite, at the interstice, at the location of Cs, and at the location of Pb, were calculated. The formation energy of the Pb defect showed to be always the lowest, which indicates that Yb^{3+} will tend to occupy the Pb^{2+} site.²⁵ Since Pb and Yb have different valences, 2+ and 3+ respectively, the charge difference needs to be compensated upon incorporation of Yb^{3+} in the lattice. Milstein *et al.* suggest that the charge is balanced by the introduction of Pb vacancies (V_{Pb}) in the perovskite nanocrystals.²³ A charge-neutral $\text{Yb}^{3+}\text{-V}_{\text{Pb}}\text{-Yb}^{3+}$ defect complex is suggested to substitute three Pb ions, as is shown in Figure 1.3.

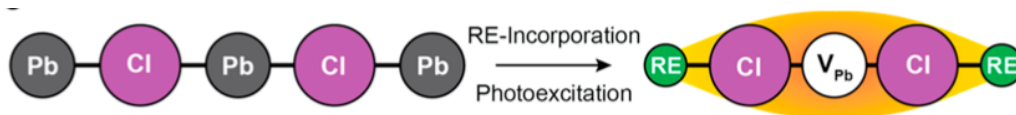


Figure 1.3. Proposed charge-neutral vacancy-defect structure for trivalent doped lanthanides in CsPbCl_3 . Figure taken from Ref. 23.

In this way the vacancy and the two Yb^{3+} ions are in close proximity, which provides sufficient electronic coupling to both ions for efficient simultaneous excitation of both.²³ This is because V_{Pb} -localized photogenerated charge carriers have a large Bohr radius as a shallow defect and therefore it spans the vacancy-defect complex, which aids the electronic transition from the host to both Yb^{3+} ions simultaneously.²³

Erickson *et al.* modelled two different structures for down-conversion: the $\text{Yb}^{3+}\text{-V}_{\text{Pb}}\text{-Yb}^{3+}$ defect complex and a structure where it involves any two Yb^{3+} ions within a given $\text{Yb}^{3+}\text{:CsPbX}_3$ nanocrystal.³⁰ In the first scenario, the effective quantum cutting rate constant is linearly correlated to the number of ground state Yb^{3+} ions. In the second scenario there was no linear correlation with the Yb^{3+} ions concentration and many more possible pairwise combinations were possible at higher concentrations.³⁰ The latter contradicts their experimental results, showing that the PLQY is linearly correlated with the Yb^{3+} concentration.³⁰ Therefore, it is most likely that the down-conversion mechanism involves the $\text{Yb}^{3+}\text{-V}_{\text{Pb}}\text{-Yb}^{3+}$ defect complex that promote fast energy transfer to the two Yb^{3+} ions within the complex.

Li *et al.* conducted DFT studies to calculate the energies of different configurations to identify the atom structure of Yb^{3+} -doped CsPbCl_3 .³² Their results were comparable with the results of Erickson *et al.*: the configurations with the $\text{Yb}^{3+}\text{-V}_{\text{Pb}}\text{-Yb}^{3+}$ defect complex showed lower energies than random dispersion of a Pb vacancy with two Yb^{3+} ions. They suggested that the $\text{Yb}^{3+}\text{-V}_{\text{Pb}}\text{-Yb}^{3+}$ complex with right-angle configuration is the most stable, followed by the linear configuration.³² However, the small energy differences between those configurations could also lead to a coexistence of these two structures. They further compared those two configurations and found that the right-angle configuration is more likely to form than the linear one, since the former causes distortion in less octahedra of the perovskite than the latter, as is shown in Figure 1.4.³²

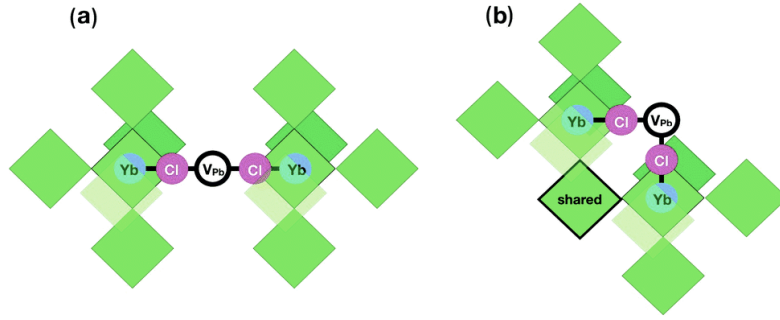


Figure 1.4. Two possible defect-complex configurations as suggested by Li *et al.* (a) Introduction of Yb^{3+} in the perovskite lattice in the linear configuration involves ten distorted octahedra. (b) Doping Yb^{3+} in a right-angle fashion involves nine distorted octahedra since one is shared between two doped structures. Figure taken from Ref. 22.

1.3 Quantum cutting in Yb^{3+} -doped CsPbCl_3

Previous studies on the dynamics of the energy transfer that enables the population of two $\text{Yb}^{2}\text{F}_{5/2}$ states in the perovskite host after excitation of the perovskite have determined that this process occurs on a picosecond time scale.^{23,24} Since this is much faster than expected for normal exciton-dopant Dexter-type energy transfer, the exciton depopulation leading to Yb^{3+} sensitization must occur via an alternative route.²³

Two different mechanisms are proposed for the energy transfer between the CsPbCl_3 and the Yb^{3+} ions, of which a schematic is shown in Figure 1.5.

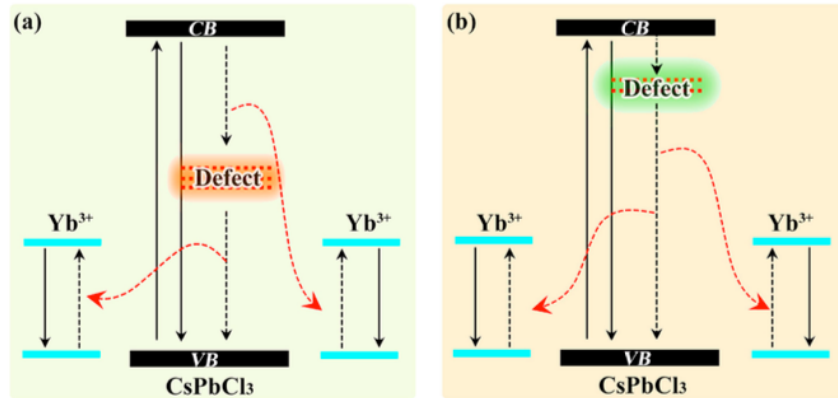


Figure 1.5. Schematic representation of two proposed mechanisms for energy transfer in $\text{Yb}^{3+}:\text{CsPbCl}_3$. (a) Energy is transferred from the perovskite to the Yb ions via a deep defect around the middle of the bandgap based on findings by Pan *et al.* (b) QC mechanism that involves a shallow defect state induced by the Yb ions as proposed by Milstein *et al.* Figure taken from Ref. 32.

Pan *et al.* proposed a mechanism that involves a deep defect around the middle of the bandgap of the perovskite.²⁵ The depopulation of the photoexcited perovskite results in the population of a defect state coupled to excitation of one $^2\text{F}_{5/2}$ states. Subsequently another electron decays from the defect state to the valence band of the host lattice, releasing another quantum of energy to excite a second $^2\text{F}_{5/2}$ states.²⁵ According to Pan *et al.* their experimental data supports this hypothesis of a deep defect state by showing an additional broadband component at 596 nm (2.08 eV) at lower temperatures. However, this emission is at an energy much larger than an intermediate energy level between the valence and conduction band of the perovskite and was also not seen at room temperature.

Milstein *et al.* suggest a mechanism that involves a shallow lattice defect induced by Yb that rapidly localizes excitation energy in the surroundings of the Yb activators.²³ Picosecond energy localization by such a defect is followed by energy transfer from the defect to a pair of neighboring Yb^{3+} ions, resulting in the emission of two near-infrared (NIR) photons.²³ The nonradiative energy transfer process that de-

excites the host and simultaneously excites two Yb^{3+} ions appears to occur on the time scale of 1 ps.²³ Their model is supported by their experimental results showing emission right below the bandgap, that is not observed for undoped systems.²³ The formation of a dopant-induced shallow trap is related with the charge-compensating defect $\text{Yb}^{3+}\text{-V}_{\text{Pb}}\text{-Yb}^{3+}$ as described before. The proximity of the defect to two Yb^{3+} ions provide sufficient electronic coupling for efficient simultaneous excitation of both.

The computational study using DFT by Li *et al.* supported the mechanism involving a shallow defect state. They found that the lanthanide doping induces variation in the valence band (VB) of undoped CsPbCl_3 rather than inducing a shallow defect level below the conduction band (CB).³² The Pb atom, associated with the right angle $\text{Yb}^{3+}\text{-V}_{\text{Pb}}\text{-Yb}^{3+}$ defect complex, would localize the photogenerated electron for the down-conversion mechanism.³²

Based on literature the quantum cutting mechanism in $\text{Yb}^{3+}:\text{CsPbCl}_3$ concerns an alteration induced by the Yb dopants, that could either be a shallow defect level below the CB or a variation in the VB. In this way an excitonic transition from the photoexcited perovskite host to the Yb ions is possible, which results in an $^2\text{F}_{5/2}$ excited state. This transition from $^2\text{F}_{7/2}$ to $^2\text{F}_{5/2}$ is very unlikely to happen since it is a Laporte forbidden transition. However, quantum cutting facilitates this excitation and subsequently two low energy photons are emitted by the Yb ions.

2. Cathodoluminescence imaging

The emission spectra and the carrier dynamics of CsPbCl_3 are examined with cathodoluminescence (CL), an electron-based spectroscopy technique. CL is a powerful method to provide nanoscale information about the optical and electronic properties of luminescent materials. This Chapter gives a brief explanation of electron microscopy and the mechanisms behind CL generation, after which the experimental set-up for both collecting CL emission spectra and time-correlated CL measurements is described.

2.1 Electron microscopy

Electron microscopy allows the study of materials at the nanoscale, since the small wavelength of the electron wavefunction (~ 7 pm for a 30 keV electron) compared to that of light (300 – 800 nm) results in a much higher spatial resolution than conventional optical microscopy.^{33,34} The use of fast electrons (0.1 keV – 300 keV of energy per electron) as an optical excitation source allows for deep-subwavelength spatial characterization.³³ The interaction of these fast electrons with the sample results in the occurrence of several processes, as depicted in Figure 2.1, which can give more information on the properties of the material and is studied by various analytical electron microscopy techniques.³⁴ After excitation with a fast electron, different electron-based signals can be detected. In a scanning electron microscope (SEM) we can detect secondary electrons (SE), that contain information about the surface topology as done in a typical SEM image, or more energetic backscattered electrons (BSE), that carry information about the atomic number and therefore the composition of the material.^{33,35} Electrons that are transmitted through the sample can also be used for microscopy, in for example transmission electron microscopy (TEM), scanning transmission electron microscopy (STEM) or electron energy loss spectroscopy (EELS).³³ High-energy electrons can also generate electromagnetic radiation that spans a broad spectrum from x-rays to the mid-IR.³⁵

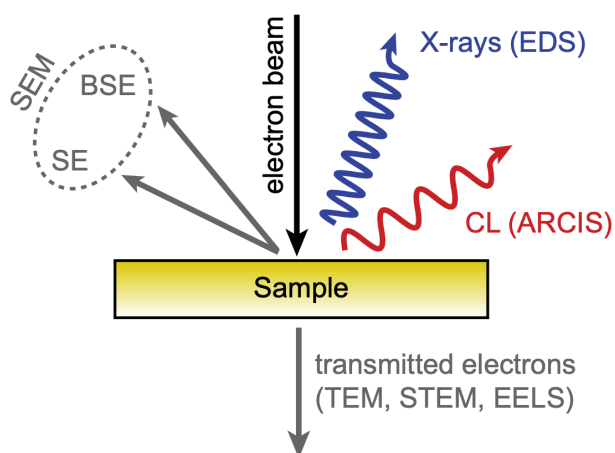


Figure 2.1. Schematic of different type of processes that appear after irradiation by energetic electrons. Different characterization techniques are given alongside the different electron-based signals. Figure taken from Ref. 33.

2.1.1 Incoherent cathodoluminescence

The electromagnetic radiation that is emitted after excitation by high energy electrons in the visible and near-infrared (NIR) regime of the spectrum is referred to as CL.^{33,34} CL emission can be divided in two types, coherent and incoherent CL, depending on the mechanism of electron excitation and light emission.³⁴ Coherent CL, in which the evanescent electric fields of the moving electron can coherently couple to far field radiation when interacting with a polarizable material, is outside the scope of this thesis.^{33–35} Incoherent CL on the other hand refers to the spontaneous emission of light after excitation with fast electrons.³⁴ The incoming electron acts as a source of energy inside the material, which can be interpreted as analogue to photons as the initial excitation source in photoluminescence (PL).³⁵ Each high energy electron gives rise to a range of primary excitations inside the material, predominantly in

the form of bulk plasmons, with energies in the tens of electron-volt (eV).³⁵ In a semiconductor, these bulk plasmons can subsequently decay into multiple charge carriers, with energies of only a few times the band gap energy, that thermalize and can diffuse and recombine.^{35,36} The recombination can lead to the emission of a photon with energy of the band gap. Hence, one energetic electron can create multiple photons, as a cascade of excitation events is created by the incident electron.^{33,35,36} Moreover, the high energy of electrons compared to photons allows for excitation of transitions with higher energy with respect to PL.³⁴ The cross sections for electron impact excitation are also different from those for optical excitation and both these factors can result in different mechanisms occurring in PL and CL.³³

CL spectroscopy can be used to give information about band edge recombination, the presence of defects in a material, atomic transitions and the chemical composition.³⁴ The nanoscale size of the tightly focused electron beam enables precise lateral characterization of the sample.³³ Altering the electron energy results in a change of the penetration depth of electrons inside a material, which can give more information about the 3D features of the material.³³ Incoherent CL, combining the study of luminescence with the high spatial resolution of the electron beam, allows for identification of localized excitation that can be presented in emission spectra maps with great detail.

2.2 Experimental set-up

In this section the different used CL techniques used for the purposes of the project are discussed. First, the cathodoluminescence imaging spectroscopy set-up is explained, after which the time-correlated single photon counting set-up is described.

2.2.1 CL spectroscopy

The most common method to study incoherent CL emission is by analyzing its spectral features, which can give valuable information on for example band edge recombination.³⁴ CL measurements on the perovskite structures were performed in a Thermo Fisher Quanta 650 scanning electron microscope (SEM) equipped with a Schottky field emission gun (FEG). During the experiments, a continuous beam of electrons, with an acceleration voltage of 30 keV, was focused onto the sample in the vacuum chamber of the SEM. The sample was deposited on a lacey carbon TEM grid and placed on a stage holder. A parabolic mirror was mounted above the sample, such that the emitted CL could be collected, as shown in Figure 2.2. This mirror was aligned with respect to the sample by using four piezoelectric stepper motors as well as varying the SEM stage height for vertical alignment of the sample.³³ The mirror was positioned such that its focal point corresponded to the focal point of the electron beam.

The parabolic mirror redirects the collimated emission out of the chamber into the Delmic Sparc Spectral system, which contains optics that focus the collected light onto a Newton CCD camera (Oxford instruments). For the alignment of the mirror the angular pattern of emission is observed using the CCD camera. A flip mirror along the optical path allows to redirect the CL emission to a fiber-coupled device, such as an external spectrometer or a set-up for time-correlated measurements, which is explained later. A schematic the set-up is shown in Figure 2.2.

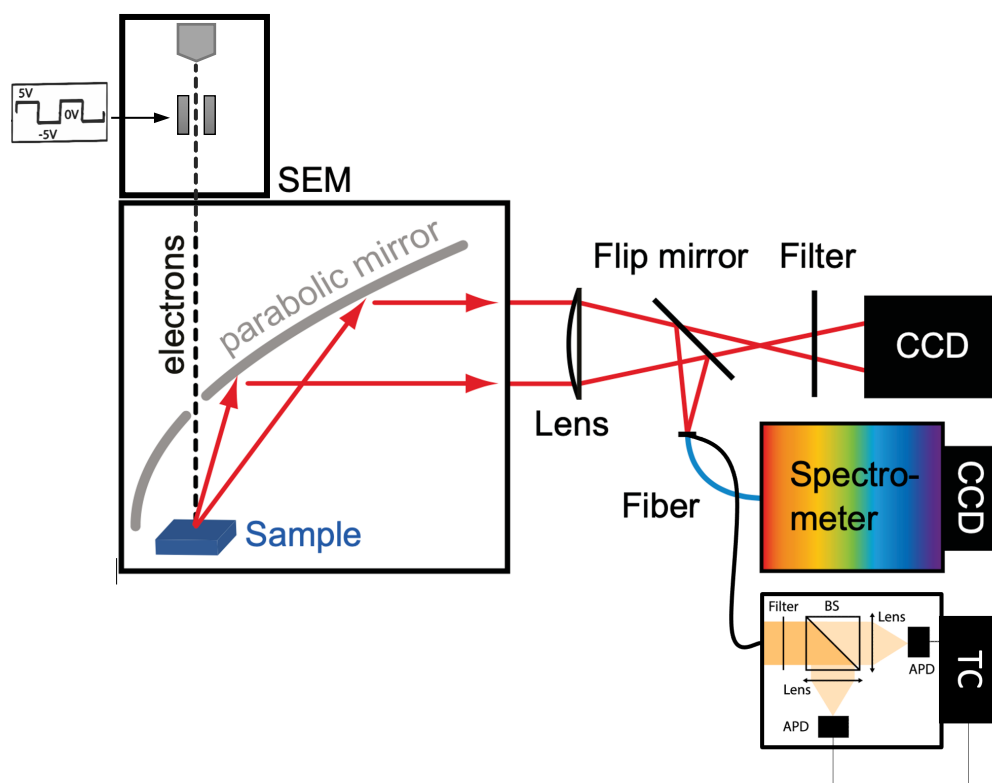


Figure 2.2. Schematic overview of the SEM chamber with the parabolic mirror and the optical components outside the chamber. The CL emitted by the sample upon excitation with electrons is directed with a flip mirror to either a fiber outcoupled device, the spectrometer or the set-up for time-correlated measurements with a time correlator (TC), or to the CCD in the Delmic Sparc Spectral system. For the time-correlated measurements the beam can be blanked with the ultrafast electrostatic blander configuration. Figure modified from Ref. 33.

Measurements are performed using the ODEMIS software to raster-scan the electron beam over a region of interest. In this way spectra for each excitation position and secondary electrons are simultaneously detected to build up a SEM image alongside the spectral scan so that CL features can be correlated to geometrical features. For visible (VIS) spectroscopy the CL emission is focused onto the Newton CCD in the Delmic Sparc Spectral system. To maintain a balance between spectral resolution and luminescence intensity a slit of $150\ \mu\text{m}$ is used, and the collected CL is directed grating before being sent to the CCD.

For the analysis of spectra in both the visible and near-infrared range an outcoupled spectrometer (Acton SP-2300i, Princeton Instruments) with a liquid-nitrogen-cooled silicon CCD array is used. This spectrometer is connected to the system via a $550\ \mu\text{m}$ diameter core multimode fiber. Depending on the region of interest a $150\ \text{g/mm}$ grating with either blaze $500\ \text{nm}$ or $800\ \text{nm}$ is used.

2.2.2 Time-resolved cathodoluminescence

CL analysis is typically used to obtain maps of the emission spectrum of a material. However, CL analysis can also give more information about the excitation and emission dynamics of emitters.³⁴ In time-resolved CL (TRCL) measurements the luminescence intensity as a function of time can be studied. To create a time-dependent luminescence intensity profile the sample is excited with a pulsed electron beam.³⁴ One method to generate a pulsed electron beam is by blanking the electron beam, in which the beam is swept across a small aperture such that the beam is effectively cut.³⁴ The electron beam is deflected by applying a pulsed voltage to a set of electrostatic plates, which can lead to temporal resolution in the picosecond range. Limitation in the temporal resolution are mainly caused by the jitter in the electronics and the rise time of the electric pulse.³⁴ The CL emission is directed to an avalanche photodiode that is connected to a time correlator. The time correlator records the exact arrival time of the emitted photons relative to the excitation pulse with the Time-Correlated Single Photon Counting (TCSPC) method.³⁷ The “start” is triggered by the excitation pulse and the arrival of a photon at the

detector causes the “stop” signal.³⁷ Repeating these “start-stop” measurements over many excitation cycles makes it possible to build up a histogram of the recorded time differences. Subsequently the luminescence lifetime can be extracted from the histogram of the decay statistics by mathematical means.³⁷ This process is schematically shown in Figure 2.3.

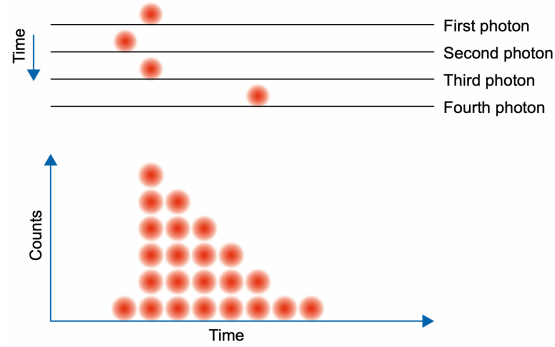


Figure 2.3. Schematic representation of the principle behind TCSPC. The exact arrival of emitted photons relative to the excitation pulse are detected and all the recorded time differences are displayed as a histogram. Figure taken from Ref. 37.

By combining the CL lifetime with the CL spectra and SEM image of a specific area, detailed information of local variations can be examined. With TRCL imaging variations in luminescence lifetime can report more on variations in electronic structure or environment by mapping decay differences.

2.2.2.1 Time-correlated single photon counting set-up

In our set-up TRCL measurements are performed by using a pulsed electrostatic blanker configuration, an aperture (70 μm) and the fiber coupled set-up for time-correlated measurements as shown in Figure 2.2. The pulsed CL emission is focused into an optical fiber (105 μm diameter core multimode fiber). The fiber guides the luminescence into an optical cart that is isolated from light. The light first passes through an adjustable neutral density filter, after which it is filtered for the perovskite emission by using a short pass 424 nm optical filter, a beam splitter and subsequently a band pass optical filter with a central wavelength of 400 nm with a bandwidth of 70 nm and hereafter it reaches the avalanche photodiode (APD). This APD is connected to a time correlator (PicoHarp 300) that is also connected to a waveform generator. The waveform generator is also connected to the ultrafast electrostatic beam blanker configuration which allows to set the desired blanking conditions. The waveform generator sends a trigger to the time correlator for every electron pulse, which indicates the “start” of the measurement and when a photon is detected by the APD this results in a “stop” signal. In this way the temporal behavior of single photons can be measured with picosecond precision, as described in section 2.2.2.

TCSPC has an inherent bias because multiple photons can arrive at the same time between two consecutive pulses. In this case only the first photon is recorded and used for the histogram, because of the “dead” time of the detector. During this time the detector cannot process another event. It is essential that this bias is minimized to guarantee that the histogram of photon arrivals represents the actual decay trace and an over-representation of early photons in the histogram is prevented.³⁷ To do so the average count rate at the detector should be at most a few percentage of the excitation rate.³⁷

2.2.2.2 Time-Tagged Time-Resolved data acquisition

The studied lifetimes for this thesis occur at very different timescales, ranging from picoseconds (ps) for the band edge recombination of CsPbCl_3 to hundreds of microseconds (μs) for the $f-f$ transition in Yb^{3+} ions. This broad range of lifetimes require different settings for the TRCL measurements. The previous described set-up is very well suited for shorter lifetimes, however due to limitations of the time correlator, TCSPC measurements are not possible for longer lifetimes, since 33 μs is the maximum full-

scale range for these measurements. Therefore, a different type of data acquisition is used for the longer lifetime of Yb³⁺ within the same set-up. The Time-Tagged Time-Resolved (TTTR) method of the PicoHarp 300 allows recording of individual events with precise information of their arrival time. In contrast to TCSPC, the TTTR mode enables access to the arrival time of each event with respect to the overall experiment time.³⁷ In this way it is possible to cover large time spans and measure the full photon emission dynamics of carriers with longer lifetimes.

To filter for the Yb³⁺ emission a long pass 900 nm filter was used. We use the T2 mode as time-tagging mode, in which all signal inputs are functionally identical and the arrival time of signals is measured on an absolute time scale.³⁷ With T2 the elapsed time since the start of the measurement and the channel at which an event has been detected are recorded.³⁷ By setting the frequency for the electrostatic beam blanker with the waveform generator, that is also connected to the time correlator, a sync pulse is recorded every time an electron pulse is given. By collecting both the time of the electron pulses and the absolute time of the arrived photons in different channels, the time between excitation by the electron beam and the detection of an emitted photon can be deduced. A visual explanation of this is given in Figure 2.4.

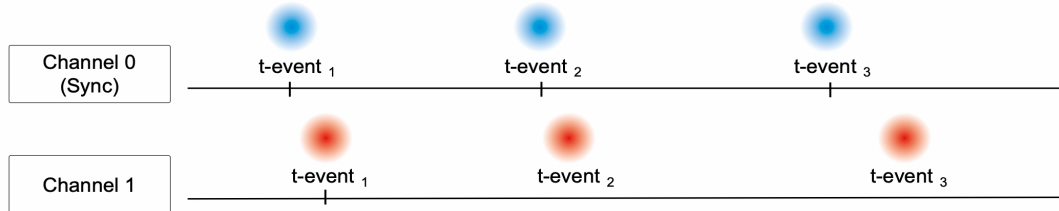


Figure 2.4. Visual representation of data collection in T2 mode. Every time an electron pulse is given this is recorded in the Sync or Channel 0. Every time a photon is detected this event receives a ‘time tag’ in Channel 1: the absolute arrival time is recorded. By subtracting the absolute time of Channel 0 (blue) from Channel 1 (red), the relative time between pulse and emitted can be found. Figure modified from Ref. 37.

By collecting all the relative times of incoming photons after pulsed excitation, a histogram can be made, by subtracting the absolute time of the of the last recorded electron pulse in Channel 0 from the absolute arrival time of the photons in Channel 1. From this histogram information about the decay dynamics can be extracted.

2.2.2.3 Second-order autocorrelation ($g^{(2)}(\tau)$)

Each high energy electron gives rise to a range of primary excitations inside the material, and thus multiple initial photons are generated per incident electron, as explained in section 2.1.1.³⁸ The second-order autocorrelation function ($g^{(2)}(\tau)$) can give more insights on these photon statistics and fundamental properties of the electron-matter interaction.^{36,38} This function describes the probability for two emitted photons to be separated by a certain time delay τ and can be measured with the fiber outcoupled time-correlated set-up as depicted in Figure 2.2.³⁹ For these measurements both APD’s 2 are used in a Hanbury Brown and Twiss (HBT) measurement. In this way, we detect the delay between two photons and subsequently build up a ($g^{(2)}(\tau)$) curve.^{38,40} In particular, it has been shown that in CL ($g^{(2)}(\tau)$) measurements exhibit photon bunching, due to the fact that multiple photons are emitted per incoming electron.^{38,40} The precise characteristics of this bunching peak depend on the electron current, the lifetime of the emitter and the probability of excitation by the electron.³⁹ As the electron beam current is known the lifetime and the excitation efficiency can be extracted from the $g^{(2)}$ data and give more insights in the electron-matter interaction.

2.3 Impact of electron beam on perovskites

With the high spatial resolution of CL measurements local variations can be measured and can give more information at the nanoscale. In this way more understanding of the local carrier dynamics of doped perovskites can be gained. However, perovskite materials have stability issues and are considered

as beam-sensitive materials.²¹ A constant concern associated with electron beam analysis of perovskite is what effect the beam has on the material properties being probed.⁴¹ All inorganic perovskites, as used in this study, display a higher resistance to electron-beam damage than its organic-inorganic counterparts.²¹ Still, previous studies on all-inorganic halide perovskites report on structural phase transformation or degradation as a result of the electron irradiation.^{21,41} Different kind of damage mechanisms, such as electron beam heating and irradiation damage, affect the defect concentration, chemical composition and phase structure of perovskites during electron-beam characterizations.²¹ As an effect of this, CL spectral peaks can be quenched, broadened, shifted or cause new peaks to appear.¹⁸ It is therefore important that irradiation conditions are carefully controlled to avoid any significant beam damage.¹⁸ Several studies suggest to reduce acceleration voltage and incident beam current for CL experiments on perovskites.^{18,21,41} The use of a pulsed electron beam is also found to be favorable, since the duration of beam irradiation on the sample is minimized.¹⁹ TRCL, as is used in this work, makes use of ultrafast electron pulses with discrete numbers of electrons per pulse.¹⁷

Another possibility to protect the perovskites against severe effects of the electron beam is by encapsulating them. This study makes use of perovskite nanocrystals (NCs) encapsulated in silica (SiO_2) molecular sieves, that were fabricated by Sarah Gillespie and Linde van de Ven from the Nanoscale Solar Cells group at AMOLF. The perovskites are made from precursors CsCl and PbCl_2 , and in the case of the doped variants also YbCl_3 or EuCl_3 is used. Those precursors are ground into the sieves after which they are calcinated at high temperatures, completely closing the porous channels, as is shown in Figure 2.5. Further information about the synthesis is outside the scope of this thesis, but further information can be found in reference 42. Electron beam studies on encapsulated perovskite NCs in silica sieves can gain insights into the stability of this matrix and the perovskites.

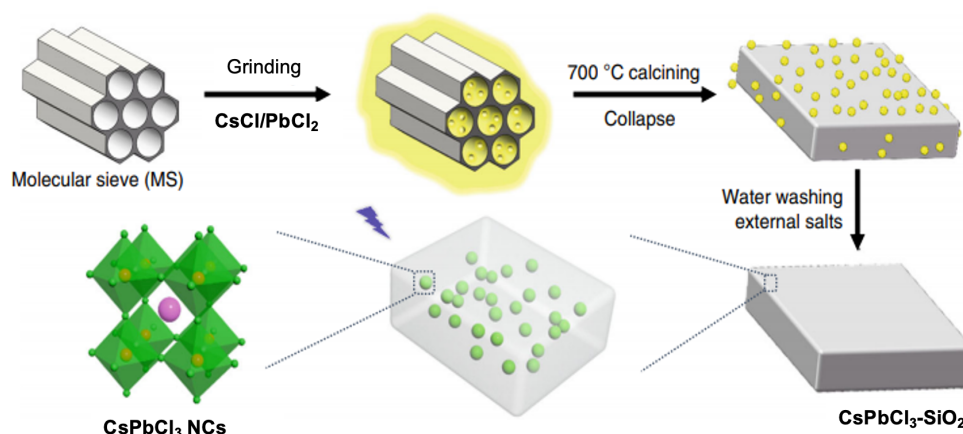


Figure 2.5. Fabrication of perovskite nanocrystals in silica molecular sieves. Figure modified from Ref. 43.

3. Results & Discussion

In this Chapter the different experimental results are presented and discussed. First, the structure of the molecular sieves and nanocrystals are observed using secondary electron images. Subsequently the CL emission spectra and CL intensity maps of CsPbCl₃, Eu³⁺-doped CsPbCl₃, Yb³⁺-doped CsPbCl₃ and the Yb₂O₃ reference sample are discussed. To get more insights on quantum cutting in Yb³⁺-doped CsPbCl₃, CL intensity and saturation trends are discussed based on spectral measurements at different currents compared to the undoped perovskite. Hereafter the decay dynamics and the TR-CL maps of CsPbCl₃ and Yb³⁺-doped CsPbCl₃ are discussed. Finally, the measured CL lifetime of the Yb³⁺ $^2F_{5/2} \rightarrow ^2F_{7/2}$ transition is discussed. This Chapter will conclude with a brief explanation on efforts made performing CL ($g^{(2)}(\tau)$) measurements.

3.1 Secondary electron images of molecular sieves

Measurements with the SEM allow for very detailed images at a nanoscale. Figure 3.1 shows three secondary electron images at different scales taken of different samples.

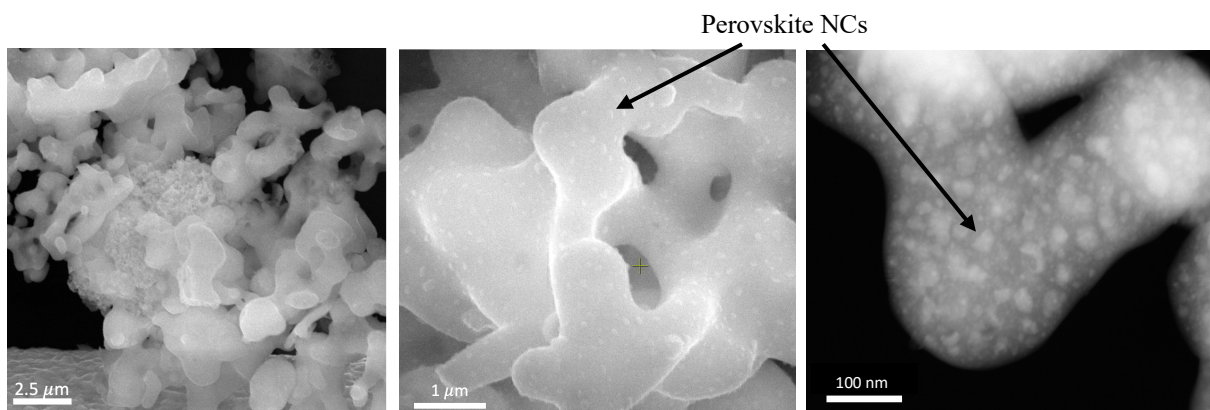


Figure 3.1. Secondary electron images in which a network of sieves is seen (left). The powder with clumps of sieves is deposited on a TEM grid, which is also visible in the bottom of the left image. In these sieves innumerable perovskite NCs are encapsulated (highlighted by the black arrows). The NCs have a different size distribution, which is clearly seen in an almost transparent sieve in the image on the right.

The network of silica molecular sieves discussed in section 2.3 form 3D clumps that are clearly visible in Figure 3.1, and are deposited on a TEM grid, which can also be seen in the bottom of the left image. The sieves encapsulate innumerable NCs, seen more clearly in the middle and right images, with a distribution of size that averages at 10 nm. CL studies on these samples have subsequently shown that before the calcining process not each channel of the sieve is filled with perovskite precursors and hence the distribution of the NCs is inhomogeneous. The 3D structure of the sieves obscures the thickness of the network, however due to the high acceleration voltage utilized (30 keV), the electron beam can penetrate and excite NCs along several micrometers of the sample. Hence, the differences in depth and the inhomogeneity of the sample will result in variations of the CL intensity, which can be related to the amount of excited NCs. However, the exact number of excited perovskite NCs cannot be derived. The encapsulation in silica sieves was found to be very successful for electron-based studies, since the samples remained stable under electron beam currents up to tens of nanoamperes. This was confirmed by exposing the perovskite to higher currents for extended periods of time and not observing drastic changes in peak intensities or the formation of novel peaks.

3.2 Spatially resolved CL emission spectra

In the following section CL emission spectra and spectral CL maps are presented for two different lanthanide-doped samples, 0.2 Eu³⁺-doped CsPbCl₃ and 0.3 Yb³⁺-doped CsPbCl₃ respectively. In this study the lanthanide concentrations are defined as the molar ratios and thus 0.3 Yb means that 1 mmol

CsCl, 1 mmol PbCl₂ and 0.3 mmol YbCl₃ were used in the synthesis. The optical and physical characteristics of the samples are compared and discussed.

3.2.1 Eu³⁺-doped CsPbCl₃

Spatially resolved CL emission spectra of encapsulated Eu³⁺-doped CsPbCl₃ NCs were measured as described in Chapter 3 and results are shown in Figure 3.2.

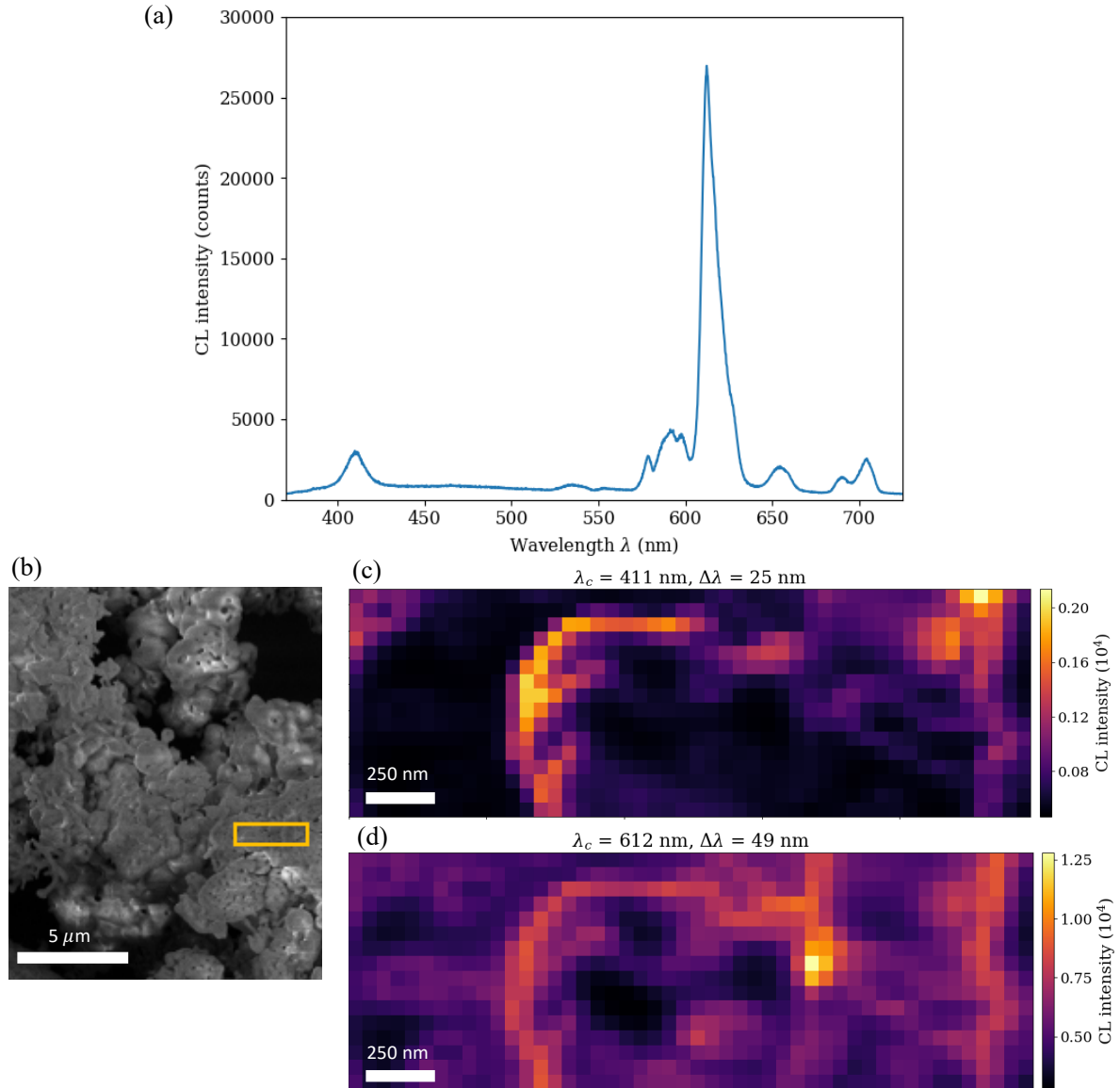


Figure 3.2. CL measurements of Eu³⁺-doped CsPbCl₃, conducted at 30 keV, 0.11 nA. (a) CL emission spectrum averaged over multiple pixels and corrected for the collection efficiency of the system (b) SEM image of a clump of sieves with encapsulated Eu³⁺-doped CsPbCl₃. The yellow box highlights the area of measurement for the spectrally resolved CL maps. (c) and (d) CL intensity maps with the perovskite band gap emission at 411 nm as central wavelength with a band width of 25 nm in (c) and the most dominant Eu³⁺ peak at 612 nm with a band width of 49 nm in (d).

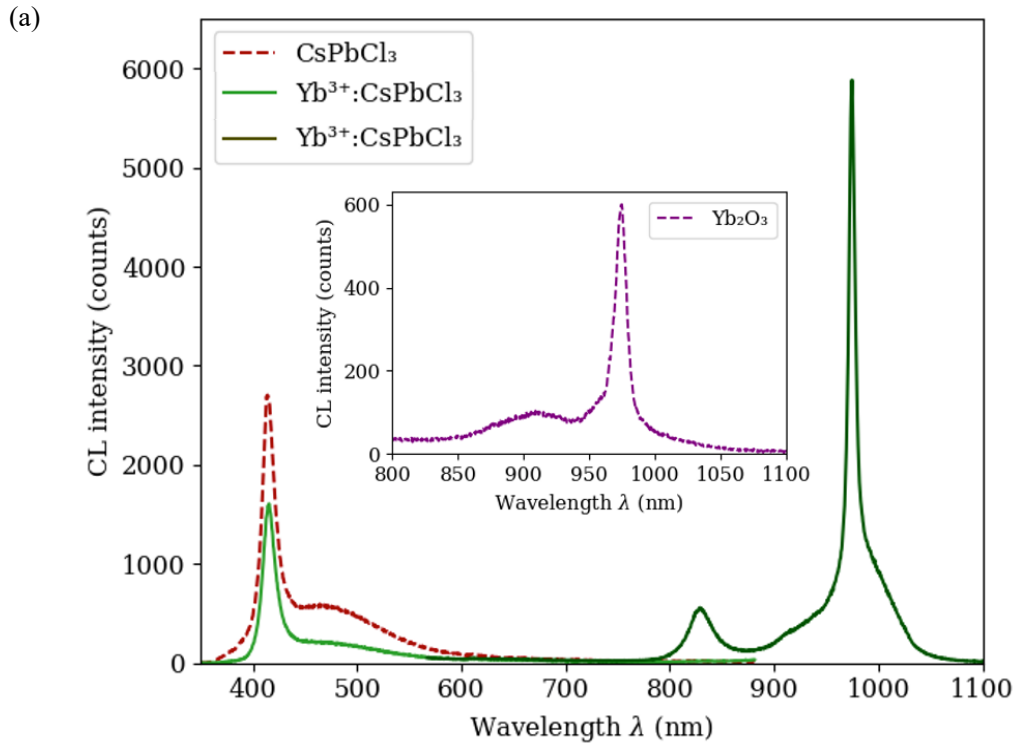
The CL spectrum in Figure 3.2 (a) shows the perovskite band gap peak at 411 nm (3.02 eV) and several Eu³⁺ transition peaks in the range of 570 – 720 nm. Eu³⁺ has multiple radiative transitions between the ⁵D₀ excited state and the ⁷F_J manifold of which the ⁵D₀ → ⁷F₂ is the most dominant at 612 nm (2.03 eV). This is an “allowed” transition and therefore the measured Eu transition peaks could be the result of both energy transfer and/or self-excitation. Quantum cutting is not possible for this system, however the energy transfer from the perovskite host to the Eu ions followed by the emission of one low energy

photon is a form of spectral shifting. From these preliminary results it remains unidentified if the emission associated with the Eu transitions is the result of excitation by energy transfer. Nevertheless, the co-localized emission from each of the species in the same area, as can be seen in the CL maps, indicates that the Eu is in close proximity to CsPbCl₃ which could suggest incorporation of the Eu ions in the perovskite lattice. This incorporation in the host lattice is required for the energy transfer and could therefore still be the mechanism that leads to population of the excited ⁵D₀ state.

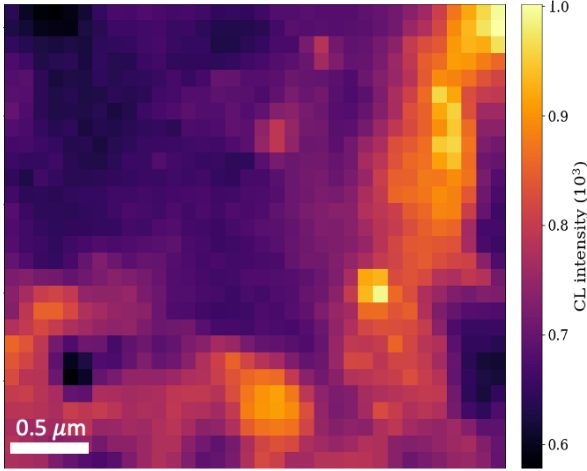
The 3D structure of the molecular sieves is also clearly visible in these CL maps, in which the beam is rastered across the sample and a CL spectrum is collected for each pixel to build up a spatial map. Not all sieves show signs of emission at the selected wavelengths, suggesting empty sieves. Emission at 612 nm and the absence of emission at 411 nm in the left side of Figure 3.2 (d) and (c) creates the impression that those sieves were not filled with CsPbCl₃ crystals, but potentially the Eu precursor is encapsulated in those molecular sieves and could self-excite and subsequently show emission.

3.2.2 Yb³⁺-doped CsPbCl₃

Unlike the Eu-doped perovskite, Yb³⁺-doped CsPbCl₃ is able to perform quantum cutting due to the favorable combination of absorption wavelength of the perovskite and the emission wavelength of the Yb. To examine if and how QC behaves in Yb³⁺-doped CsPbCl₃ NCs encapsulated in silica molecular sieves when probed with CL, several types of measurements have been conducted. To start, this section presents and discusses CL emission spectra and spectral CL maps, which are shown in Figure 3.3.



(b)

Doped CsPbCl₃: $\lambda_c = 415$ nm, $\Delta\lambda = 30$ nm

(c)

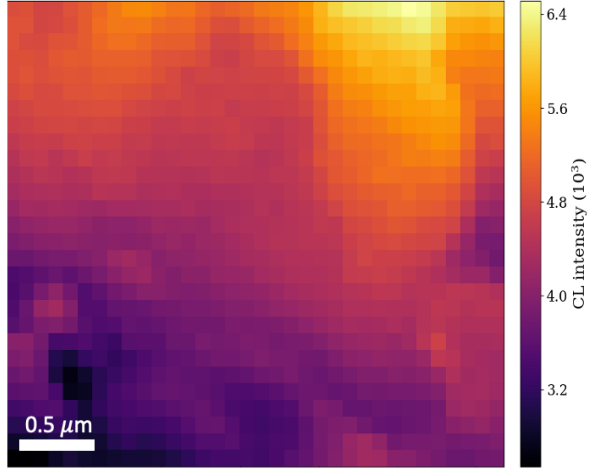
Yb³⁺: $\lambda_c = 975$ nm, $\Delta\lambda = 5$ nm

Figure 3.3. CL measurements on Yb³⁺-doped CsPbCl₃, undoped CsPbCl₃ and Yb₂O₃ all encapsulated in silica sieves, conducted at 30 keV, 0.55 nA. (a) Averaged CL emission spectra of Yb³⁺-doped CsPbCl₃ (green) and CsPbCl₃ (dotted red) and in the inset Yb₂O₃ (purple). For Yb₂O₃ a longer exposure time was chosen due to lower CL intensity. All spectra are corrected for the collection efficiency of the system (b) CL intensity map of Yb³⁺-doped CsPbCl₃ at a central wavelength of 415 nm with a band width of 30 nm. (c) CL intensity map of Yb³⁺-doped CsPbCl₃ at a central wavelength of 975 nm with a band width of 5 nm.

The CL spectrum in Figure 3.3 (a) displays the CsPbCl₃ spectrum (dashed red curve) that peaks at 414 nm. This peak can be assigned to the perovskite band gap edge. The spectrum in Figure 3.3 (a) also displays the spectrum of Yb³⁺-doped CsPbCl₃ (green curves) with peaks at 415 nm as a result of the perovskite band edge emission and at 975 nm resulting from the $^2F_{5/2} \rightarrow ^2F_{7/2}$ transition. The broad peak in the range of 440 – 570 nm can be attributed to CL emission from the silica. The shoulder of the Yb³⁺ peak in the range of 860 – 950 nm can also be attributed to the silica. The small peak at 830 nm is the second order diffraction of the perovskite band edge emission. Due to the large difference in energies between the perovskite and Yb emission, the full spectrum was obtained by performing two measurements using a grating with 500 nm and 800 nm blaze (green and dark green, respectively).

The difference in intensity between the undoped CsPbCl₃ and doped CsPbCl₃ peak is seen in all measurements as a trend. The decrease in radiative recombination suggests an increase of non-radiative processes upon doping and possibly indicates quantum cutting in the doped system. However, upon doping more defects are created, as was described in section 1.2.2, to maintain charge neutrality when Yb ions replace Pb ions, which could also be an explanation for more non-radiative recombination.

The inset of Figure 3.3 (a) shows the CL spectrum of Yb₂O₃ encapsulated in silica sieves with a peak at 975 nm, that can be assigned to the emission of Yb³⁺ ions. From measured CL spectra of Yb₂O₃ it can be concluded that the emission from the $^2F_{5/2} \rightarrow ^2F_{7/2}$ transition at 975 nm is a result of population of the $^2F_{5/2}$ state by self-excitation since there is no possibility for energy transfer from other species in this system. The self-excitation of this Laporte forbidden Yb³⁺ transition can be explained by the relatively large momentum of the electrons which allow for the excitation of transitions that are symmetry- or momentum-forbidden for plane wave excitation.^{33,35} Hence, probing optically forbidden transitions with CL should take into account different excitation mechanisms and therefore CL spectra can deviate from PL spectra. This also implies that the Yb³⁺ peak from the Yb³⁺-doped CsPbCl₃ spectrum could be the result of different excitation mechanisms, including self-excitation. The emission at 975 nm in the Yb³⁺-doped CsPbCl₃ spectrum however on order of magnitude more intense than in the Yb₂O₃ spectrum, while the measurement exposure time of the Yb³⁺-doped CsPbCl₃ is 12 times shorter than the exposure time of Yb₂O₃. This suggests the excitation of many more Yb ions and the presence of a different

excitation mechanism in the doped perovskite system, that could likely be quantum cutting. Nonetheless, this variation in intensity could also be related to different concentrations of Yb^{3+} ions.

Figure 3.3 (b) and (c) displays spectrally filtered CL intensity maps for the perovskite and Yb emission, respectively. These maps of the exact same area show both significant enhanced emission from Yb and the perovskite in the same region, which suggests incorporation of the dopant into the perovskite crystal lattice. From these maps it seems that there is a significant amount of Yb emission throughout the entire map, while for example the top left corner shows almost no emission of the perovskite. This could suggest non-radiative recombination processes for the perovskites in this area, such as energy transfer. Another possibility is the absence of perovskite NCs in this area and the emission from Yb in this area could then be possible through self-excitation of free Yb^{3+} ions in this area.

3.2.3 Trends upon increasing currents in Yb^{3+} -doped CsPbCl_3 and undoped CsPbCl_3

To gain more insights into the excitation mechanisms responsible for the emission of Yb in the Yb^{3+} -doped CsPbCl_3 spectrum, the following section looks at the effect of different currents on the samples and its emission.

3.2.3.1 Saturation trends in Yb^{3+} -doped CsPbCl_3

To measure the effect of different currents on the doped perovskite eight different areas were measured to study the changing intensities of the CsPbCl_3 band edge emission peak at 415 nm and the Yb^{3+} peak at 975. Figure 3.4 shows the several averaged spectra for different currents.

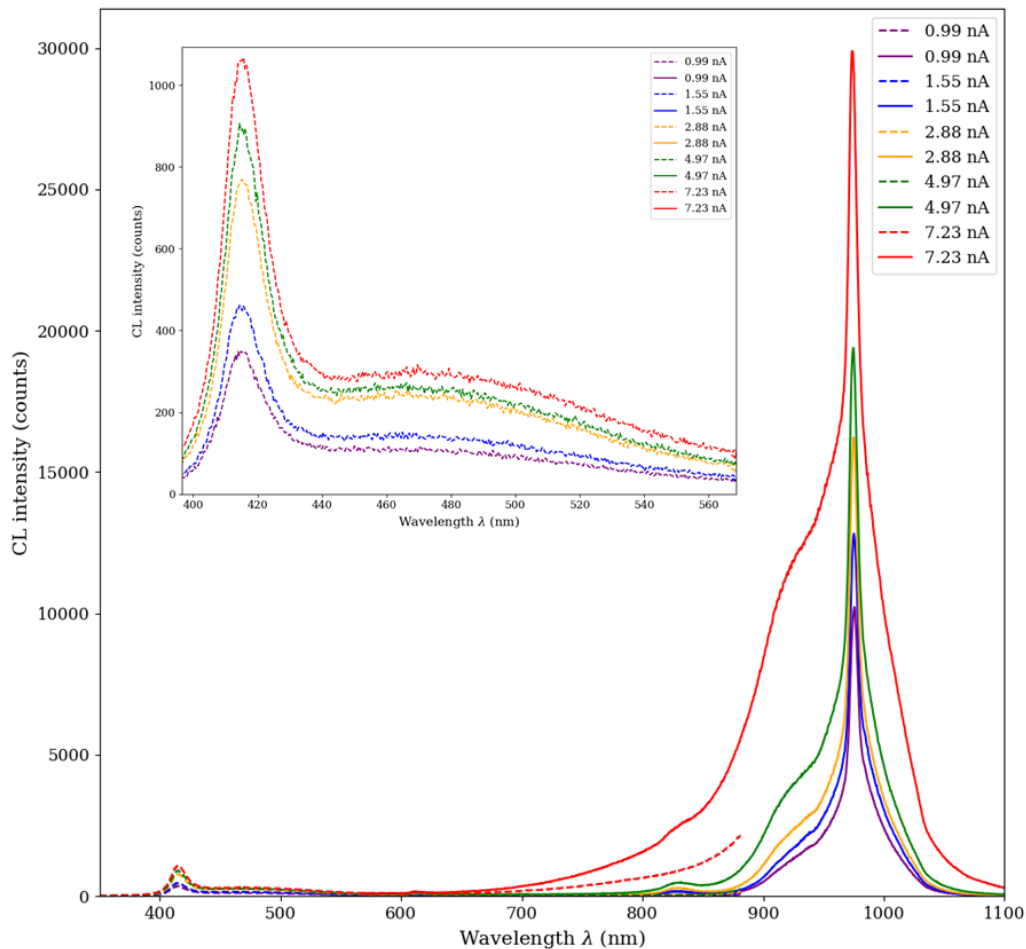


Figure 3.4. Evolution of Yb^{3+} -doped CsPbCl_3 CL spectrum as a function of increasing currents. Spectra are averaged and corrected for the collection efficiency of the system. Due to the different energy regions of emission between the perovskite and Yb emission, the full spectrum was obtained by performing two measurements using a grating with 500 nm and 800 nm blaze (dotted lines and solid lines, respectively).

Figure 3.4 displays the perovskite band gap emission at 415 nm and the Yb^{3+} emissive state at 975 nm, both at currents in the range of 0.99 to 7.23 nA. The inset of Figure 3.4 shows an enlarged image of the perovskite peak in which also the silica emission in the range of 440 – 570 nm is seen. The shoulder of the Yb^{3+} peak in the range of 860 to 950 nm can also be attributed to the silica. The second order diffraction peak of CsPbCl_3 is present at 830 nm. Upon increasing currents all peaks show increased CL intensity as was expected since more carriers can be excited. The higher currents also cause thermal broadening, as a result of electron-beam induced heating of the sample.¹⁸

The average increase of the intensity of the Yb peak with respect to the perovskite peak as function of current in doped perovskite samples is found to follow the same trend. Four different areas within the Yb^{3+} -doped CsPbCl_3 sample were measured in the range of 0.24 nA to 14 nA. The average perovskite peak at 415 and the Yb peak at 975 show to have increasing intensities till 8 nA, after which the emission saturates. This similar behavior towards increased number of electrons suggests a mutual dependence of Yb and the perovskite. The Yb transition has a much longer lifetime than the perovskite and is therefore more likely to saturate earlier. The approximately same point of saturation implies that the saturated excited state of Yb causes saturation of the perovskite, since the perovskite cannot transfer its energy to the Yb anymore. This argument is further supported in section 4.2.3.2. It is unlikely that the saturation of the perovskite dictates the saturation of Yb, since as a result of self-excitation the Yb intensity would continue to increase as a function of current. This is not seen in the results and therefore, it is assumed that the saturation of the perovskite is a result of saturation of the excited state of Yb and this trend implies energy transfer from the perovskite to the Yb. However, the extent to which energy transfer is responsible for the excitation of Yb is difficult to quantify.

3.2.3.2 Saturation trends between undoped CsPbCl_3 and Yb-doped CsPbCl_3

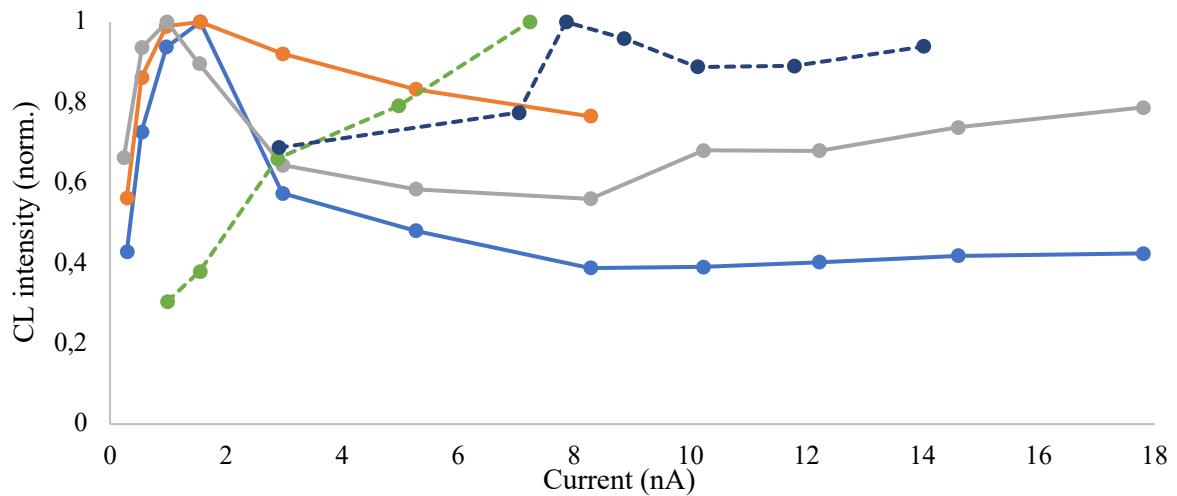


Figure 3.4. Normalized CL intensity at 415 nm as a function of current for undoped CsPbCl_3 (solid lines) and Yb-doped CsPbCl_3 (dashed lines). The different lines represent measurements on different particles and each data point is based on 50 CL spectra.

Figure 3.4 displays multiple measurements of the CL intensity at 415 nm as a function of current for both undoped and doped CsPbCl_3 . Every line represents a different measured area of the sample, and each data point represents the average CL intensity based on 50 pixels. At lower currents both doped and undoped perovskite exhibit the same trend: the intensity increases as function of the current. Around 2 nA all undoped perovskites show a remarkable drop in intensity. This could be the result of a technical issue encountered at the stage of measurements, such as misalignment of the focal point of the electron beam with respect to the parabolic mirror, that would result in a decrease in collection efficiency.⁴⁴ The doped perovskite however still shows an increase up till around 7 nA and hereafter stabilizes. The later point of saturation for the doped perovskite when compared to the undoped perovskite suggests that the doped version has more energy transfer pathways, suggesting energy transfer to Yb. Around 8 nA the Yb emission shows saturation, and it is assumed that therefore at this point the doped perovskite also

saturates. As the saturation trends as function of current show hints for energy transfer from the perovskite host to Yb, it remains unknown till what extend this excitation mechanism is competing with self-excitation of Yb by incident electrons.

3.3 Time-resolved CL decay traces and maps of CsPbCl₃

To gain more insight in the decay dynamics of doped and undoped CsPbCl₃ and the potential QC in the doped perovskite TR-CL measurements were conducted. In this section TR-CL data, obtained as explained in section 3.2.2, is presented and discussed. First the lifetime and decay traces for both doped and undoped CsPbCl₃ are discussed. Subsequently a spatial dependence of the radiative lifetime is explored using TR-CL maps.

3.3.1 Lifetimes of undoped and Yb³⁺-doped CsPbCl₃

Decay traces of undoped and doped CsPbCl₃ were measured at 9.4 pA, as is shown in Figure 3.5.

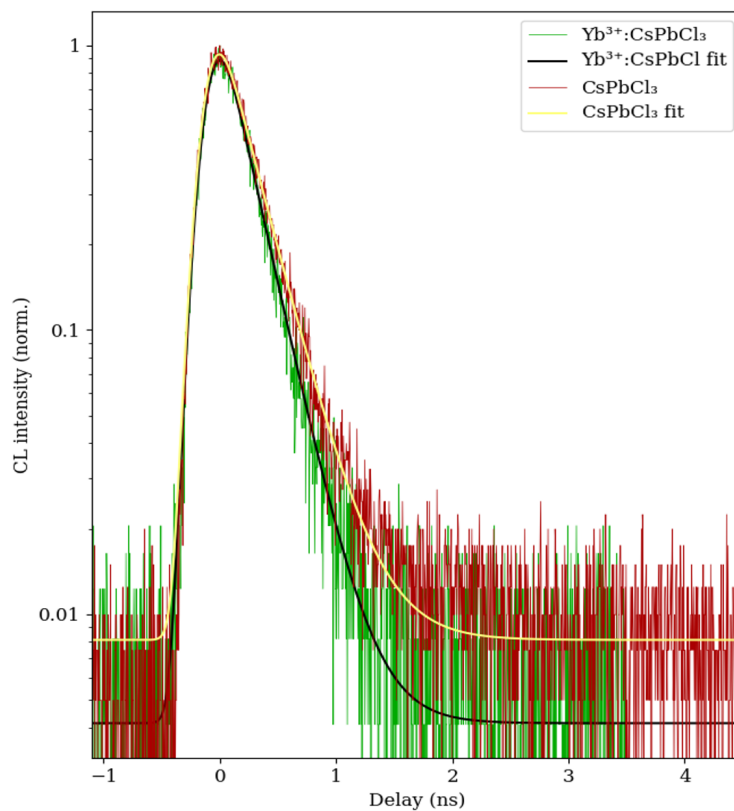


Figure 3.5. Decay traces and corresponding convolution fit of CsPbCl₃ undoped (red) and doped with Yb (green) measured at 9.4 pA with a fitted pulse width of 106 ps and 113 ps, respectively.

The measured decay traces of CsPbCl₃ could be fitted with a monoexponential decay as shown in equation 4.1.

$$I(t) = I(0)e^{-t/\tau} \quad \text{Eq. 4.1}$$

For undoped CsPbCl₃ a CL lifetime of $\tau = 261.6 \pm 5.1$ ps was determined. Measured time-resolved PL lifetimes showed results in the same time range. These lifetimes are much shorter than previously reported PL lifetimes for CsPbCl₃ in the range of 2 to 5 ns.^{9,23–25} Most likely the difference is caused by the difference in matrix. The much shorter lifetime of the perovskite NCs measured in this study suggest more dominant non-radiative recombination pathways, that could be due to the formation of more trap states as a result of encapsulation in the silica molecular sieves.

The radiative lifetime of Yb-doped CsPbCl₃ was determined to be $\tau = 232.5 \pm 4.4$ ps. We hypothesized that the lifetime of the doped perovskite would be considerably shorter than the lifetime

of the undoped perovskite, because of the non-radiative QC pathway. However, the difference in lifetime is rather small and the values are close to the resolution of the set-up, with an instrument response function in the range of 60 – 80 ps and therefore this difference should be interpreted with care. The small difference in lifetime between the doped and the undoped perovskite could suggest the introduction of new recombination pathways upon doping, such as QC. However, the slightly shorter lifetime of the doped perovskite could also be related to alteration of the chemical composition or another non-radiative pathway, as upon introduction of Yb ions into the crystal lattice more defects are created. Due to the ultrashort lifetimes and the shortcomings of the set-up at these timescales it is too complex to relate these findings to QC. Moreover, reported lifetime values of CsPbCl₃ showed different trends upon doping with Yb³⁺. Pan *et al.* and Zhang *et al.* showed a similar increase in lifetime upon doping, from ~4 ns to ~8.5 ns, while Zhou *et al.* and Milstein *et al.* both showed an increase in lifetime, from 4.5 and 2 ns to ~1.5 ns, respectively.^{9,23–25} These studies did mostly not explain these differences or did not relate their differences in lifetime upon doping to energy transfer processes.

Decay traces of CsPbCl₃ doped with Eu³⁺ were also measured and similar lifetimes as in the Yb-doped perovskite were calculated.

3.3.2 TR-CL maps of undoped and Yb³⁺-doped CsPbCl₃

To identify whether there is a correlation between the spatially variant optical response of the system and lifetime, TR-CL maps were obtained in different configurations of both undoped CsPbCl₃ and the Yb-doped CsPbCl₃. A TR-CL map of CsPbCl₃ is presented next to a CL map of the same area in Figure 3.6.

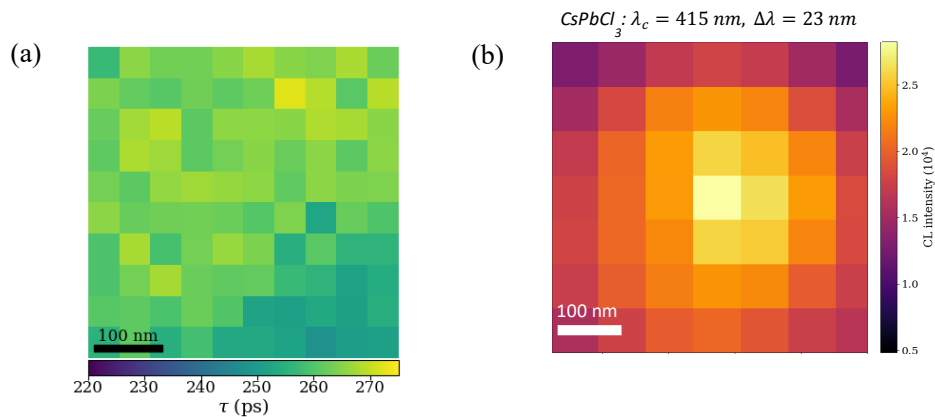


Figure 3.6. (a) TR-CL map for undoped CsPbCl₃ with lifetimes in the range of 220 to 275 ps. (b) Complementary spectrally filtered CL intensity maps of same area.

The maps in Figure 3.6 show that for an undoped perovskite sample, there is no direct relation between observed CL intensity and CL lifetime at such length scales. On the other hand, for the Yb-doped CsPbCl₃ comparing the optical response with the time-resolved data showed a consistent difference in lifetime throughout the Yb-doped CsPbCl₃ sample. In areas with higher CL intensity for the NIR Yb emissive state a longer lifetime was found ($\tau = 239.4 \pm 3.7$ ps) than in areas with low CL intensity for Yb³⁺ ($\tau = 222.5 \pm 3.7$ ps). The slightly increased lifetime may be attributed to passivation of defects by present Yb ions and therefore partly eliminating non-radiative pathways.^{24,25} However, as these differences are close to the temporal resolution of the set-up they should be interpreted with care.

3.4 Time-resolved CL decay traces of Yb³⁺

The CL lifetime of Yb³⁺ was measured by filtering for the NIR emissive state and using the T2 mode appropriate for materials with long lifetimes, the resulting decay trace is seen in Figure 3.7. The initial aim was to study the rise time of this decay trace and identify a relationship with the perovskite decay trace. However, the use of low frequency of the electron pulse resulted in very low counts at low binning and therefore the rise time could not be fitted.

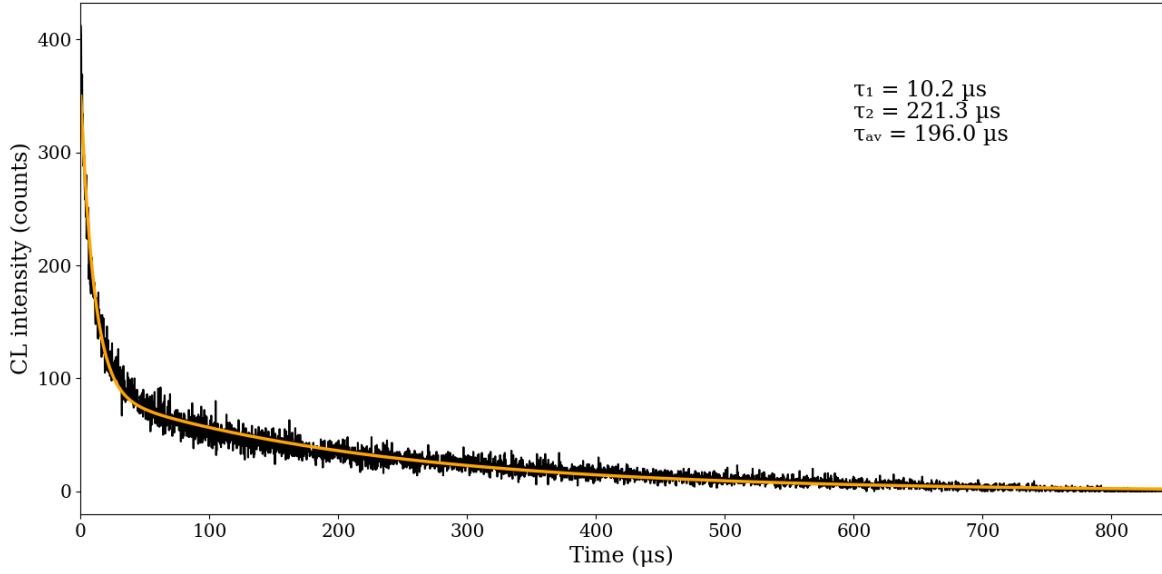


Figure 3.7. Decay trace of the $^2F_{5/2} \rightarrow ^2F_{7/2}$ transition of Yb^{3+} measured with the T2 mode at 0.20 nA and 100 Hz.

The measured emissive lifetime of the $^2F_{5/2} \rightarrow ^2F_{7/2}$ transition of Yb^{3+} could be fitted with a biexponential decay according to Eq. 4.2.

$$I(t) = a_1 e^{-t/\tau_1} + a_2 e^{-t/\tau_2} \quad \text{Eq 4.2}$$

The average calculated lifetime of Yb^{3+} is $196 \mu\text{s}$. This is shorter but comparable with values found in literature in similar systems.^{9,23–25,30,31} We observe a biexponential decay, which could be explained by the presence of two kinds of Yb^{3+} populations that each independently contribute to the overall signal with their own lifetimes, respectively $\tau_1 = 10.2 \mu\text{s}$ and $\tau_2 = 221.3 \mu\text{s}$. These lifetimes are several orders of magnitude longer than the time scales associated with the perovskite radiative lifetime, energy transfer and self-excitation and it is therefore presumable that the lifetimes are caused by a distinct property that is directly associated with the Yb^{3+} ions and their surroundings. The longer lifetime τ_2 is likely to be related to the less perturbed intrinsic Yb^{3+} symmetry forbidden $f-f$ transition that corresponds to more protected emitters that are not distorted by the perovskite host lattice.⁴⁵ It is assumed that the shorter lifetime τ_1 arises from a distortion to the Yb^{3+} symmetry upon doping in the perovskite lattice. The distortion of the Yb ions would decrease the intrinsic octahedral symmetry, which would also decrease the forbidden nature of the transition, resulting in a shorter lifetime. The different lifetimes could thus most likely be attributed to different emitting centers with each different environments in terms of geometry or neighboring transferring sites, which results in different population and emission pathways.⁴⁵ Biexponential decays have been reported in other species with forbidden transitions between symmetrical atomic orbitals, such as in manganese (Mn) doped CsPbCl_3 .

3.5 CL $g^{(2)}(\tau)$ measurements

CL $g^{(2)}(\tau)$ measurements in both continuous and pulsed electron beam conditions were carried out for the perovskite emission wavelength for Eu^{3+} -doped CsPbCl_3 and undoped CsPbCl_3 to gain more insights into the photon statistics of these samples. By measuring the probability for two emitted photons to be separated by a certain time delay τ a $g^{(2)}(\tau)$ curve could be generated.^{38,40} It has already been shown that $g^{(2)}(\tau)$ measurements in CL exhibit photon bunching, due to the fact that one electron can create multiple photons.^{38,40} From the precise characteristics of this bunching peak the lifetime and the excitation efficiency can be extracted and give understanding of material excitation and photon emission dynamics. However, despite efforts being made to find suitable conditions, no bunching was exhibited in these samples. For these measurements very low current regimes ($\sim \text{pA}$) are needed since at low electron currents the time between two electrons increases, resulting in a better separation of the photon

bunches and thus a stronger bunching peak.³⁹ However at these low currents the signal from the sample is too low to build a $g^{(2)}(\tau)$ curve. This low CL intensity can be related to the relatively low PLQY of CsPbCl₃ band gap emission.⁴² It was therefore likely that this issue would be the same for Yb³⁺-doped CsPbCl₃ and therefore $g^{(2)}(\tau)$ measurements were not performed on this particular sample. Nevertheless, it is not excluded that other perovskites, such as CsPbBr₃ with higher PLQY's, would show high enough signal to measure photon bunching with CL.

4 Conclusion & Outlook

To the best of our knowledge, this work presented for the first time spatially resolved CL emission spectra and CL decay traces of CsPbCl₃ and Yb-doped CsPbCl₃ encapsulated in a silica matrix, in order to study their optical properties and the perovskite-lanthanide energy transfer process. With the high spatial resolution of CL measurements local variations in luminescence and lifetime could be determined, providing more information about the samples at the nanoscale. The encapsulation in silica molecular sieves was found to be very successful for electron-based studies, since the samples remained stable under electron beam currents up to tens of nanoamperes. This is not only promising for high energy electron studies of perovskite, but also for perovskite stability studies in general.

Yb³⁺-doped CsPbCl₃ is able to perform quantum cutting due to the favorable combination of absorption wavelength of the perovskite and the emission wavelength of the Yb. To examine how QC behaves in Yb³⁺-doped CsPbCl₃ NCs when probed with CL, both CL emission spectra and CL decay traces were studied. The excitation of the optically forbidden excited state of the Yb ions is likely the result of both QC and self-excitation by incident high energy electrons. The results showed several indications for energy transfer from the perovskite host to the excited state of Yb, one of which being the observation of co-localized perovskite and Yb emission, suggesting the incorporation of the Yb ions into the perovskite crystal lattice. From the CL emission spectra, a consistently lower intensity was seen for the perovskite emission in the doped sample, suggesting the presence of non-radiative recombination mechanisms like QC. Similarly, the Yb emission has a much higher CL intensity with comparison to Yb₂O₃, however it is likely that the concentrations of Yb³⁺ ions in these systems differ. From studying the CL intensity as function of current it can be concluded that the doped perovskite saturates at higher currents than the undoped perovskite, also suggesting more energy transfer pathways and potentially QC. The Yb and perovskite emission in the doped CsPbCl₃ samples follow the same saturation trend, indicating that once the saturation threshold of Yb is reached, the perovskite is also subsequently saturated. The TR-CL data exhibits a slight decrease in perovskite lifetime upon doping with Yb, which could be assigned to QC, but also to other non-radiative recombination pathways via induced defects upon doping. However, since values are close to the resolution of the set-up the TR-CL data should be interpreted with care. Since quantifying the different excitation mechanisms of Yb remains unaccomplished, it remains unknown to what extent QC is responsible for excitation of the excited state of Yb. Upon doping with Yb more defects are created to maintain charge neutrality. It is unknown what the effect of these defects is on the non-radiative recombination in doped CsPbCl₃. Therefore, more research is needed on the influence of doping to determine its influence in the measured differences in this study between undoped and doped perovskite.

This study introduced the method of T2 to measure longer CL lifetimes within our set-up. The emissive lifetime of the $^2F_{5/2} \rightarrow ^2F_{7/2}$ transition of Yb³⁺ was measured and fitted with a biexponential decay. The biexponential decay could be explained by the presence of two kinds of Yb³⁺ luminescence centers, a less perturbed and a more perturbed population, which further indicates successful incorporation of the Yb ions in the perovskite crystal lattice.

For future QC studies on Yb³⁺-doped CsPbCl₃ it would be interesting to systematically study the influence of the chemical composition in CL studies. The effect of different doping concentrations could be probed to gain more insights into the effect of doping and the introduction of defects. Measuring lifetimes of doped-CsPbCl₃ in a pump-probe configuration allows for detection of femtosecond decay dynamics and could potentially help building a model for QC in Yb³⁺-doped CsPbCl₃. An attempt at conducting PL photon bunching experiments could also be interesting to gain more understanding of the photon statistics and altogether generate a knowledge framework for energy transfer processes occurring in Yb³⁺-doped CsPbCl₃.

Finally, considering the long-term prospects, the aim of this and other works on QC is contributing to the fundamental understanding and development of QC layers for solar cell applications in the foreseeable future.

Acknowledgement

I'd first like to thank Albert for giving me the opportunity to work in his group with the incredibly fascinating CL set-up. Your enthusiasm and drive to keep learning are really inspiring!

Nika, I want to thank you for everything that you have taught me during the project, I would have never thought from the beginning that I would have it in me to work with our precious Quanta on my own, thank you for always believing in me and supporting me and answering my endless questions. You truly know a lot and I really admire how invested you are and that you never give up, even if everything seems to break down all at once. Apart from that I enjoyed all the fun and good conversations we had, thank you for being such a lovely person!

Magda, my $g^{(2)}(\tau)$ goddess, where would I have been without all your insights and support. Thank you for always helping me out with all my questions and data analysis struggles and all other daily life struggles ;) You are so talent full, I really enjoyed learning from you.

I would also like to thank Matthias and Kelly for sharing all their CL knowledge and helping me out. Whenever I got stuck somewhere, you would take time to help me.

I would also like to thank Sarah and Linde for the endless discussions about the perovskites and ofcourse for always supplying me with samples!

I am incredibly grateful to have been part of the Molecular Photonics group, Andrea, Daphne, Evelijn, Hannah, Hollie, Kelly Magda, Matthias, Nika, Stefan, Tom and Verena, you all are amazing and incredibly smart. I really enjoyed all our online and offline time during these strange times! Thank you for making me feel more then welcome and all the interesting conversations we had.

Last but certainly not least, I would like to thank my family and friends for always supporting me and believing in me.

References

- (1) Fawzy, S.; Osman, A. I.; Doran, J.; Rooney, D. W. Strategies for Mitigation of Climate Change: A Review. *Environ Chem Lett* **2020**, *18* (6), 2069–2094. <https://doi.org/10.1007/s10311-020-01059-w>.
- (2) Kannan, N.; Vakeesan, D. Solar Energy for Future World: - A Review. *Renewable and Sustainable Energy Reviews* **2016**, *62*, 1092–1105. <https://doi.org/10.1016/j.rser.2016.05.022>.
- (3) Strümpel, C.; McCann, M.; Beaucarne, G.; Arkhipov, V.; Slaoui, A.; Švrček, V.; del Cañizo, C.; Tobias, I. Modifying the Solar Spectrum to Enhance Silicon Solar Cell Efficiency—An Overview of Available Materials. *Solar Energy Materials and Solar Cells* **2007**, *91* (4), 238–249. <https://doi.org/10.1016/j.solmat.2006.09.003>.
- (4) Wegh, R. T.; Donker, H.; van Loef, E. V. D.; Oskam, K. D.; Meijerink, A. Quantum Cutting through Downconversion in Rare-Earth Compounds. *Journal of Luminescence* **2000**, *87–89*, 1017–1019. [https://doi.org/10.1016/S0022-2313\(99\)00514-1](https://doi.org/10.1016/S0022-2313(99)00514-1).
- (5) Wegh, R. T.; Donker, H.; Oskam, K. D.; Meijerink, A. Visible Quantum Cutting in LiGdF₄:Eu³⁺ through Downconversion. *Science* **1999**, *283* (5402), 663–666. <https://doi.org/10.1126/science.283.5402.663>.
- (6) Dexter, D. L. Possibility of Luminescent Quantum Yields Greater than Unity. *Phys. Rev.* **1957**, *108* (3), 630–633. <https://doi.org/10.1103/PhysRev.108.630>.
- (7) Sark, W. G. J. H. M. van; Meijerink, A.; Schropp, R. E. I. *Solar Spectrum Conversion for Photovoltaics Using Nanoparticles*; IntechOpen, 2012. <https://doi.org/10.5772/39213>.
- (8) Richards, B. S. Enhancing the Performance of Silicon Solar Cells via the Application of Passive Luminescence Conversion Layers. *Solar Energy Materials and Solar Cells* **2006**, *90* (15), 2329–2337. <https://doi.org/10.1016/j.solmat.2006.03.035>.
- (9) Zhou, L.; Liu, T.; Zheng, J.; Yu, K.; Yang, F.; Wang, N.; Zuo, Y.; Liu, Z.; Xue, C.; Li, C.; Cheng, B.; Wang, Q. Dual-Emission and Two Charge-Transfer States in Ytterbium-Doped Cesium Lead Halide Perovskite Solid Nanocrystals. *J. Phys. Chem. C* **2018**, *122* (47), 26825–26834. <https://doi.org/10.1021/acs.jpcc.8b07906>.
- (10) Boix, P. P.; Agarwala, S.; Koh, T. M.; Mathews, N.; Mhaisalkar, S. G. Perovskite Solar Cells: Beyond Methylammonium Lead Iodide. *J. Phys. Chem. Lett.* **2015**, *6* (5), 898–907. <https://doi.org/10.1021/jz502547f>.
- (11) Norris, D. J.; Efros, A. L.; Erwin, S. C. Doped Nanocrystals. *Science* **2008**, *319* (5871), 1776–1779. <https://doi.org/10.1126/science.1143802>.
- (12) Mir, W. J.; Sheikh, T.; Arfin, H.; Xia, Z.; Nag, A. Lanthanide Doping in Metal Halide Perovskite Nanocrystals: Spectral Shifting, Quantum Cutting and Optoelectronic Applications. *NPG Asia Mater* **2020**, *12* (1), 1–9. <https://doi.org/10.1038/s41427-019-0192-0>.
- (13) Rare-earth doped materials enhance silicon solar cell efficiency <https://www.spie.org/news/3701-rare-earth-doped-materials-enhance-silicon-solar-cell-efficiency> (accessed 2021 -09 -21).
- (14) Luo, X.; Ding, T.; Liu, X.; Liu, Y.; Wu, K. Quantum-Cutting Luminescent Solar Concentrators Using Ytterbium-Doped Perovskite Nanocrystals. *Nano Lett.* **2019**, *19* (1), 338–341. <https://doi.org/10.1021/acs.nanolett.8b03966>.
- (15) Zhou, D.; Liu, D.; Pan, G.; Chen, X.; Li, D.; Xu, W.; Bai, X.; Song, H. Cerium and Ytterbium Codoped Halide Perovskite Quantum Dots: A Novel and Efficient Downconverter for Improving the Performance of Silicon Solar Cells. *Advanced Materials* **2017**, *29* (42), 1704149. <https://doi.org/10.1002/adma.201704149>.
- (16) Zhou, Y.; Chen, J.; Bakr, O. M.; Sun, H.-T. Metal-Doped Lead Halide Perovskites: Synthesis, Properties, and Optoelectronic Applications. *Chem. Mater.* **2018**, *30* (19), 6589–6613. <https://doi.org/10.1021/acs.chemmater.8b02989>.
- (17) Wai, R. B.; Ramesh, N.; Aiello, C. D.; Raybin, J. G.; Zeltmann, S. E.; Bischak, C. G.; Barnard, E.; Aloni, S.; Ogletree, D. F.; Minor, A. M.; Ginsberg, N. S. Resolving Enhanced Mn²⁺ Luminescence near the Surface of CsPbCl₃ with Time-Resolved Cathodoluminescence Imaging. *J. Phys. Chem. Lett.* **2020**, *11* (7), 2624–2629. <https://doi.org/10.1021/acs.jpcclett.0c00574>.
- (18) Xiao, C.; Li, Z.; Guthrey, H.; Moseley, J.; Yang, Y.; Wozny, S.; Moutinho, H.; To, B.; Berry, J. J.; Gorman, B.; Yan, Y.; Zhu, K.; Al-Jassim, M. Mechanisms of Electron-Beam-Induced Damage in Perovskite Thin Films Revealed by Cathodoluminescence Spectroscopy. *J. Phys. Chem. C* **2015**, *119* (48), 26904–26911. <https://doi.org/10.1021/acs.jpcc.5b09698>.

- (19) Orri, J. F.; Tennyson, E. M.; Kusch, G.; Divitini, G.; Macpherson, S.; Oliver, R. A.; Ducati, C.; Stranks, S. D. Using Pulsed Mode Scanning Electron Microscopy for Cathodoluminescence Studies on Hybrid Perovskite Films. *Nano Ex.* **2021**, 2 (2), 024002. <https://doi.org/10.1088/2632-959X/abfe3c>.
- (20) Coenen, T.; Haegel, N. M. Cathodoluminescence for the 21st Century: Learning More from Light. *Applied Physics Reviews* **2017**, 4 (3), 031103. <https://doi.org/10.1063/1.4985767>.
- (21) Ran, J.; Dyck, O.; Wang, X.; Yang, B.; Geohegan, D. B.; Xiao, K. Electron-Beam-Related Studies of Halide Perovskites: Challenges and Opportunities. *Advanced Energy Materials* **2020**, 10 (26), 1903191. <https://doi.org/10.1002/aenm.201903191>.
- (22) Ferro, S. M.; Wobben, M.; Ehrler, B. Rare-Earth Quantum Cutting in Metal Halide Perovskites – a Review. *Mater. Horiz.* **2021**, 8 (4), 1072–1083. <https://doi.org/10.1039/D0MH01470B>.
- (23) Milstein, T. J.; Kroupa, D. M.; Gamelin, D. R. Picosecond Quantum Cutting Generates Photoluminescence Quantum Yields Over 100% in Ytterbium-Doped CsPbCl₃ Nanocrystals. *Nano Lett.* **2018**, 18 (6), 3792–3799. <https://doi.org/10.1021/acs.nanolett.8b01066>.
- (24) Zhang, X.; Zhang, Y.; Zhang, X.; Yin, W.; Wang, Y.; Wang, H.; Lu, M.; Li, Z.; Gu, Z.; Yu, W. W. Yb³⁺ and Yb³⁺/Er³⁺ Doping for near-Infrared Emission and Improved Stability of CsPbCl₃ Nanocrystals. *J. Mater. Chem. C* **2018**, 6 (37), 10101–10105. <https://doi.org/10.1039/C8TC03957G>.
- (25) Pan, G.; Bai, X.; Yang, D.; Chen, X.; Jing, P.; Qu, S.; Zhang, L.; Zhou, D.; Zhu, J.; Xu, W.; Dong, B.; Song, H. Doping Lanthanide into Perovskite Nanocrystals: Highly Improved and Expanded Optical Properties. *Nano Lett.* **2017**, 17 (12), 8005–8011. <https://doi.org/10.1021/acs.nanolett.7b04575>.
- (26) Tilley, R. J. D. Lanthanoid Ion Color. In *Encyclopedia of Color Science and Technology*; Luo, M. R., Ed.; Springer: New York, NY, 2016; pp 827–834. https://doi.org/10.1007/978-1-4419-8071-7_257.
- (27) Werts, M. H. V.; Jukes, R. T. F.; Verhoeven, J. W. The Emission Spectrum and the Radiative Lifetime of Eu³⁺ in Luminescent Lanthanide Complexes. *Phys. Chem. Chem. Phys.* **2002**, 4 (9), 1542–1548. <https://doi.org/10.1039/B107770H>.
- (28) Van Gosen, B. S.; Verplanck, P. L.; Seal II, R. R.; Long, K. R.; Gambogi, J. *Rare-Earth Elements*; Professional Paper; USGS Numbered Series 1802-O; U.S. Geological Survey: Reston, VA, 2017; Vol. 1802-O, p 44. <https://doi.org/10.3133/pp1802O>.
- (29) Feenstra, J.; Six, I. F.; Asselbergs, M. A. H.; Leest, van, R. H.; Wild, de, J.; Meijerink, A.; Schropp, R. E. I.; Rowan, A. E.; Schermer, J. J. Er³⁺/Yb³⁺ Upconverters for InGaP Solar Cells under Concentrated Broadband Illumination. *Physical Chemistry Chemical Physics* **2015**, 2015 (17), 11234–11243. <https://doi.org/10.1039/c4cp03752a>.
- (30) Erickson, C. S.; Crane, M. J.; Milstein, T. J.; Gamelin, D. R. Photoluminescence Saturation in Quantum-Cutting Yb³⁺-Doped CsPb(Cl₁–XBr_x)₃ Perovskite Nanocrystals: Implications for Solar Downconversion. *J. Phys. Chem. C* **2019**, 123 (19), 12474–12484. <https://doi.org/10.1021/acs.jpcc.9b01296>.
- (31) Klimentov, D.; Dvoyrin, V. V.; Halder, A.; Paul, M. C.; Das, S.; Bhadra, S. K.; Sorokina, I. T. Emission Decay and Energy Transfer in Yb/Tm Y-Codoped Fibers Based on Nano-Modified Glass. *Optical Materials* **2015**, 42, 270–275. <https://doi.org/10.1016/j.optmat.2014.12.045>.
- (32) Li, X.; Duan, S.; Liu, H.; Chen, G.; Luo, Y.; Ågren, H. Mechanism for the Extremely Efficient Sensitization of Yb³⁺+Luminescence in CsPbCl₃ Nanocrystals. *J. Phys. Chem. Lett.* **2019**, 10 (3), 487–492. <https://doi.org/10.1021/acs.jpcclett.8b03406>.
- (33) Coenen, T. *Angle-Resolved Cathodoluminescence Nanoscopy*; 2014.
- (34) Solà-Garcia, M. *Electron-Matter Interaction Probed with Time-Resolved Cathodoluminescence*; 2021.
- (35) Brenny, B. J. M. *Probing Light Emission at the Nanoscale with Cathodoluminescence*; 2016.
- (36) Solà-Garcia, M.; Mauser, K. W.; Liebrau, M.; Coenen, T.; Christiansen, S.; Meuret, S.; Polman, A. Photon Statistics of Incoherent Cathodoluminescence with Continuous and Pulsed Electron Beams. *ACS Photonics* **2021**, 8 (3), 916–925. <https://doi.org/10.1021/acsp Photonics.0c01939>.
- (37) Wahl, M. Time-Correlated Single Photon Counting. 14.
- (38) Meuret, S.; Tizei, L. H. G.; Cazimajou, T.; Bourrellier, R.; Chang, H. C.; Treussart, F.; Kociak, M. Photon Bunching in Cathodoluminescence. *Phys. Rev. Lett.* **2015**, 114 (19), 197401. <https://doi.org/10.1103/PhysRevLett.114.197401>.
- (39) Meuret, S.; Coenen, T.; Woo, S. Y.; Ra, Y.-H.; Mi, Z.; Polman, A. Nanoscale Relative Emission Efficiency Mapping Using Cathodoluminescence g(2) Imaging. *Nano Lett.* **2018**, 18 (4), 2288–2293. <https://doi.org/10.1021/acs.nanolett.7b04891>.
- (40) Meuret, S.; Solà Garcia, M.; Coenen, T.; Kieft, E.; Zeijlemaker, H.; Lätzel, M.; Christiansen, S.; Woo,

- S. Y.; Ra, Y. H.; Mi, Z.; Polman, A. Complementary Cathodoluminescence Lifetime Imaging Configurations in a Scanning Electron Microscope. *Ultramicroscopy* **2019**, *197*, 28–38. <https://doi.org/10.1016/j.ultramic.2018.11.006>.
- (41) Guthrey, H.; Moseley, J. A Review and Perspective on Cathodoluminescence Analysis of Halide Perovskites. *Advanced Energy Materials* **2020**, *10* (26), 1903840. <https://doi.org/10.1002/aenm.201903840>.
- (42) Gillespie, S. *Encapsulating Metal Halide Perovskite Nanocrystals in Silica Molecular Sieves*; 2021.
- (43) Zhang, Q.; Wang, B.; Zheng, W.; Kong, L.; Wan, Q.; Zhang, C.; Li, Z.; Cao, X.; Liu, M.; Li, L. Ceramic-like Stable CsPbBr₃ Nanocrystals Encapsulated in Silica Derived from Molecular Sieve Templates. *Nat Commun* **2020**, *11* (1), 31. <https://doi.org/10.1038/s41467-019-13881-0>.
- (44) Brenny, B. J. M.; Coenen, T.; Polman, A. Quantifying Coherent and Incoherent Cathodoluminescence in Semiconductors and Metals. *Journal of Applied Physics* **2014**, *115* (24), 244307. <https://doi.org/10.1063/1.4885426>.
- (45) Lu, H.; Peng, Y.; Ye, H.; Cui, X.; Hu, J.; Gu, H.; Khlobystov, A. N.; Green, M. A.; Blower, P. J.; Wyatt, P. B.; Gillin, W. P.; Hernández, I. Sensitization, Energy Transfer and Infra-Red Emission Decay Modulation in Yb³⁺-Doped NaYF₄ Nanoparticles with Visible Light through a Perfluoroanthraquinone Chromophore. *Sci Rep* **2017**, *7* (1), 5066. <https://doi.org/10.1038/s41598-017-05350-9>.
- (46) Yuan, X.; Ji, S.; De Siena, M. C.; Fei, L.; Zhao, Z.; Wang, Y.; Li, H.; Zhao, J.; Gamelin, D. R. Photoluminescence Temperature Dependence, Dynamics, and Quantum Efficiencies in Mn²⁺-Doped CsPbCl₃ Perovskite Nanocrystals with Varied Dopant Concentration. *Chem. Mater.* **2017**, *29* (18), 8003–8011. <https://doi.org/10.1021/acs.chemmater.7b03311>.